DETECTION AND ASSESSMENT OF HIGH TEMPERATURE HYDROGEN ATTACK IN STEEL PRESSURE VESSELS USING NON-COLLINEAR WAVE MIXING

BY

JOHN FRANCIS CONWAY II

THESIS

Submitted in partial fulfillment of the requirements
for the degree of Master of Science in Systems and Entrepreneurial Engineering
in the Graduate College of the
University of Illinois at Urbana-Champaign, 2017

Urbana, Illinois

Adviser:

Professor Henrique Reis

ABSTRACT

High temperature hydrogen attack (HTHA) is a problem that has been affecting energy related systems such as coal gasifiers and fuel processors for a long time. HTHA can result in sudden, catastrophic failures that are costly and dangerous. Prevention of this type of damage is of paramount importance, however no current detection technique is capable of non-destructively and reliably assessing the level of damage in HTHA affected vessels. This study presents a nondestructive testing approach that is capable of evaluating HTHA damage in pressure vessels made of carbon steels. A strategy of detection involving non-collinear wave mixing of ultrasonic waves and pulse-inversion is illustrated using a test sample extracted from a retired pressure vessel. Results show that nonlinear ultrasonics are capable of detecting and evaluating HTHA damage over the thickness of the specimen. These results are then compared to tensile tests conducted on tensile specimens machined from various depths through the thickness of the retired pressure vessel. The reduction in strength of the machined tensile specimens correlates well with nonlinear ultrasonic measurements, showing the reliability and validity of this method for inspection. The non-collinear wave mixing technique can be used with access only to the outside surface of a pressure vessel which makes this strategy appealing for in-situ inspection.

For my brother Kevin

ACKNOWLEDGMENTS

I would like to express my deepest gratitude for everyone who has helped me through the last few years in graduate school. I would not have been able to accomplish as much as I have without a great number of people. Many thanks to my current lab mates, Punyaslok Rath, He Wang, Josh Love, and Lihui Sun. We have had a lot of great times together, goofing around in and out of the lab. I will always cherish those memories. I would also like to specifically thank Megan McGovern, none of my research would have been possible without your suggestions, advice, and helpfulness. I would also like to thank my advisor, Professor Reis. I am very grateful for you inviting me into your lab and for giving me the opportunity to work on this project. You have given me valuable advice and guidance for both academics and my life. I am truly grateful to have worked with you during my time in graduate school. Additionally a special thanks goes out to the American society for Nondestructive Testing for the graduate student fellowship, which provided funding for this project. I also need to thank Dr. David Farrow who provided helpful advice and access to testing equipment, making this project possible. I also need to thank Mr. James Mabon, Mr. C.Q. Chen and Ms. Jade (Zhiyu) Wang, from the Materials Research Lab, for helping me in obtaing the scanning electron microscopic images. I greatly appreciate the time each of you spent helping me. And lastly, I would like to thank my parents, who have always supported me. You have provided me with so much, I cannot thank you enough.

TABLE OF CONTENTS

LIST OF TABLES vi

LIST OF FIGURES vii

CHAPTER 1 INTRODUCTION 1
1.1 Problem 1
1.2 Objectives 3
1.3 Description of Experimentation 4
1.4 Overview 6

CHAPTER 2 LITERATURE REVIEW 7
2.1 Hydrogen Damage in Steels 7
2.2 HTHA Detection 10
2.3 Non-Collinear Wave Mixing 13

CHAPTER 3 METHODOLOGY 16
3.1 Non-Collinear Wave Mixing 16
3.2 Pulse Inversion 21
3.3 Nonlinear Parameter 23

CHAPTER 4 EXPERIMENTAL PREPARATION AND PROCEDURES 25
4.1 Linear Acoustic Characterization 25
4.2 Non-Collinear Wave Mixing Configuration 32
4.3 Tensile Testing 35
4.4 Microscopy 39

CHAPTER 5 RESULTS 40
5.1 Non-Collinear Wave Mixing Results 40
5.2 Tensile Strength Results 43
5.3 Microscopy 50

CHAPTER 6 CONCLUSION 55

CHAPTER 7 FUTURE RECOMMENDATIONS 57
7.1 Single Sided In-situ Inspection 57
7.2 Collinear Wave Mixing for Nonlinear Interrogation of Steel 58

REFERENCES 63

LIST OF TABLES

4.1 Shear and longitudinal wave velocities and attenuations at the inside surface, outside surface, the mean and the predicted inside surface values calculated from Equation 4.9. Extracted from McGovern [1] 30

5.1 Results from tensile tests 46

LIST OF FIGURES

1.1 Examples of pressure vessels, heat exchangers and pipping equipment at a refinery, which may be susceptible to HTHA damage. Extracted from [2]. . 2
1.2 Severely HTHA damaged heat exchanger with large rupture caused by sudden catastrophic failure. Extracted from [3]. 3

2.1 Illustration of an API 941 Nelson Curve, showing two different steel types. Extracted from [4, 5] 9

3.1 Simple representation of intersecting waves, case a represents a non-collinear collision that results in a sum frequency. Case b represents a non-collinear interaction with a difference frequency. 17

4.1 Bare test specimen, showing large cracks running through the center. 25
4.2 Typical set up for single transducer pulse-echo probing. 26
4.3 Longitudinal subsurface wave measurement configuration. θ_{inc} must be set to the first critical angle governed by Snell's law in order to induce critically refracted waves [6]. 28
4.4 Dilatational and shear ultrasonic attenuation coefficients (Np/m) through the thickness of the damaged pressure vessel. Equation 4.9 is plotted as a dashed line is plotted for dilatational attenuation and solid line is plotted for shear attenuation. The Open circles plotted on each curve are the average of ten separate measurements taken at the outside surface, through the thickness, and the inside surface. The error bars correspond to the maximum and minimum values obtained during experimentation. This figure was extracted with permission, from McGovern et al. [1]. 32
4.5 Testing configuration schematic diagram for non-collinear wave mixing with a pulse inversion technique. 33
4.6 Testing configuration, showing both A545S-5M 3.5 MHz primary wave transducers, and the 7.5 MHz Olympus V121 receiving transducer. 34
4.7 Geometry of machined tension specimen. 35
4.8 Illustration of tensile specimen locations within the test piece. 37
4.9 Tensile specimen loaded in the Instron model 4400 load frame with the extensometer attached and centered. 38
4.10 Microscopic imaging configuration. The JEOL 7000F analytical Scanning electron microscope is pictured. 39

5.1 Plot a shows the time domain record of simultaneous operation of both primary transducers, plot b shows the time domain record of the inverted simultaneous operation of both transducers, Plot c shows the summation of Plots a and b, and Plot d shows the filtered plot of the summation. Note that the expected arrival time is shown. 41
5.2 Normalized nonlinear wave generation parameter versus the distance from the outside surface. Note that the error bars overlap since distances between measurement depths are smaller than the characteristic length of the interaction region. The shape of the normalized nonlinear wave generation parameter versus distance illustrates the pattern of HTHA damage through the thickness of the pressure vessel wall. 42
5.3 Stress Strain relationships for all tensile tests from specimen set one, excluding 1.5 and 1.6 due to severe damage. 44
5.4 Stress Strain relationships for all tensile tests from specimen set two, excluding 2.4, 2.5 and 2.6 due to severe damage. 44
5.5 This figure illustrates the stress-strain relationship for specimens 1.1, 1.2, and 1.8. Note the distinct difference between the strength values of each specimen. 45
5.6 Figure illustrates the stress-strain relationship for specimens 2.1 and 2.8. Note the distinct difference between the strength values of each specimen. . . 45
5.7 Estimation of yield strength by identifying the point where the stress-strain curve deviates from linearity. 47
5.8 Normalized nonlinear wave generation parameter and percent reduction in yield strength versus distance from the outside surface. This figure illustrates the relative reduction in yield strength with an increase of the nonlinear wave generation parameter. 48
5.9 Normalized nonlinear wave generation parameter and percent reduction in ultimate strength versus distance from the outside surface. This Figure illustrates the relative reduction in ultimate strength with an increase of the nonlinear wave generation parameter. 49
5.10 This image displays 20x magnification a large macroscopic crack which runs through the specimen, additionally numerous small cracks and voids can be seen below the larger crack. The location of this image is roughly 1 cm from the inside surface. 51
5.11 This image displays a 50x magnification of the region below the large crack (closer to the inside surface) filled with numerous voids and small fissures. . 52
5.12 This image displays a 200x magnification of the region below the large crack (closer to the inside surface). 53
5.13 This image displays a 750x magnification of a particular microcrack found in 5.12. Note that the dark regions around the microcrack display a pearlitic microsctructure composition. 54

7.1 Schematic representation of a potential alternative configuration for single sided nonlinear interrogation of HTHA. 59

7.2 Schematic representation of a potential alternative configuration for single sided nonlinear interrogation of HTHA using a wave guide and angled wedges. 61

CHAPTER 1

INTRODUCTION

1.1 Problem

High temperature hydrogen attack (HTHA) is a form of damage that can occur in process equipment that is exposed to hydrogen at high temperatures and pressures. This type of equipment includes heat exchangers, piping equipment, and pressure vessels (see Figure 1.1). HTHA damage can rapidly deteriorate a steel pressure vessel which can lead to dangerous and catastrophic failures. However, through extensive research on this issue, efforts to mitigate this problem have been made in the form of Nelson curves [5]. These curves represent empirical strategies in place to ensure safe design and operation of pressure vessels subject to high temperature and high partial pressures of hydrogen. Despite these regulations, HTHA still remains a problem due to excitations in pressure and temperature levels above normal operating conditions. There are numerous material compositions available to construct steel pressure vessels, including carbon, Mo and Cr-Mo steels, to name a few. These steels all have microstructures containing carbides. Though these alloying components can help the mechanical properties of steel, they are also partially responsible for initiating HTHA [7].

HTHA damage is the result of hydrogen diffusing into steel and bonding with carbon atoms to form small micro bubbles of methane [2, 7, 8]. These bubbles can coalesce along grain boundaries and form larger fissures, which can further progress into significant tears and cracks within the material. By this point, an HTHA affected pressure vessel can become extremely dangerous. For example, an incident resulted in a heat exchanger within a Tesoro Anacortes Refinery to rupture, shown in Figure 1.2. This sudden rupture released

Figure 1.1: Examples of pressure vessels, heat exchangers and pipping equipment at a refinery, which may be susceptible to HTHA damage. Extracted from [2].

Figure 1.2: Severely HTHA damaged heat exchanger with large rupture caused by sudden catastrophic failure. Extracted from [3].

a gaseous mixture that ignited and fatally injured seven employees. The cause of this incident was determined to be HTHA damage to the heat exchanger [3, 9]. Due to incidents like this, there is a significant need to detect this type of damage in its early stages, in order to prevent further catastrophes from occurring. Unfortunately, it is difficult to detect HTHA until it has developed into advanced stages where it becomes dangerous. Traditional methods are unreliable and are not practical in large scale damage detection within affected steel [10].

1.2 Objectives

The best conclusive option to diagnose HTHA at early onset has been through microstructural analysis. This type analysis can show evidence of methane bubble formation in microscopic images. However, microscopic inspection can only take place if a pressure vessel can be properly prepared and examined with proper equipment. Although microscopy can provide adequate damage analysis after taking a vessel out of service, it is not ideal for in-situ inspection, i.e. microscopy is not practical or economical for in-situ inspection. The difficulties surrounding this problem have spurred significant efforts to develop techniques that can perform non-destructive evaluation of pressure vessels. Many methods have been attempted, and many have shown to detect HTHA fissures, including

attenuation comparisons, spectral analysis, backscatter techniques, and traditional linear ultrasonic techniques. However in rigorous testing, these methods have been shown to be unreliable and impractical for reasonable scanning procedures [10]. Because of issues with the accuracy and success of these methods, the in-situ testing of operational pressure vessels still remains a challenge today. The ability to measure the presence of HTHA in operational pressure vessels would be invaluable to users and operators in terms of both safety and life-cycle decisions on components.

The objective of this study is to show the effectiveness and reliability of using non-collinear wave mixing as a detection technique for HTHA damage in steel pressure vessels and to show that non-collinear wave mixing can be a powerful characterization and evaluation tool for HTHA damage assessment in test specimens. Furthermore, a technique called pulse inversion [11] will also be utilized during non-collinear wave mixing. This technique can improve detection capabilities of non-collinear wave mixing by increasing the amplitude of the nonlinear signal. Coinciding with the nonlinear interrogation of the damaged steel, tensile strength testing will also be conducted on specimens cut from the same damaged steel pressure vessel to correlate the measured degree of damage to the reduction in tensile strength. Lastly, microscopic images of the cross section of the steel pressure vessel have been produced using an electron scanning microscope to verify and show the manifestation of the damage near the inside diameter of the steel pressure vessel.

1.3 Description of Experimentation

As mentioned above, non-collinear wave mixing will be the primary focus of HTHA detection in the steel testing specimen. Non-collinear wave mixing is a form of nonlinear ultrasonic testing. Nonlinear ultrasonic testing differs from conventional ultrasonic testing techniques and offers different advantages in many cases. Traditional ultrasonics relies primarily on the reflection and transmission of sound waves in materials. These techniques often have resolutions too low to detect HTHA damage. Whereas, nonlinear ultrasonics, specifically non-collinear wave mixing, relies on interactions between propagating sound

waves within a medium. These interactions are highly sensitive to the presence of local nonlinearities such as small micro fissures. This makes non-collinear wave mixing an attractive and promising method for the identification of HTHA damage.

Prior to attempting nonlinear interrogation through the use of non-collinear wave mixing, it was necessary to obtain testing specimens that have been subject to significant HTHA damage. Fortunately for this study, extensively damaged specimens have been obtained from the same pressure vessel, allowing for the application and comparison between the techniques mentioned above. Additionally, preparations must be made to the specimen in order to run the non-collinear tests. Preparations include polishing and linear ultrasonic characterization. Details on these preparations will be further discussed in Chapter 4, Experimental Preparation and Procedures.

After the necessary preparations, non-collinear wave mixing is completed by intersecting two shear waves within the specimen thickness to produce a nonlinear scattered dilatational wave. The amplitude of the nonlinear scattered wave are then measured with a receiving transducer after it had traveled from the region of interaction. The peak to peak amplitude of the nonlinear scattered wave is proportional to the degree of nonlinearity within the specimen [12], and therefore, the degree of HTHA damage. The resulting amplitudes are then normalized and compared across the thickness of the specimen.

In addition to non-collinear wave mixing, tensile strength testing has been completed on steel tensile specimens created from a damaged section of the same steel pressure vessel that was inspected with non-collinear wave mixing. Tensile specimens are tested for their ultimate tensile strength, showing the reduction in strength relative to the depth through the thickness in which the machined tensile specimen came from. After the strength testing was completed on specimens from throughout the thickness, results from nonlinear interrogation and the strength testing are compared to show the corresponding relationship.

Finally, scanning electron microscopic images have been taken of the cross section of a third specimen originating from the same steel pressure vessel. Damaged areas are

displayed and analyzed.

1.4 Overview

Chapter 2 provides literature reviews that are relevant to the studies performed. These reviews will cover the history of HTHA damage and HTHA damage detection using ultrasonic techniques. Additionally, Non-collinear wave mixing will be discussed in more detail, including other applications and the specific case that will be used in these studies.

Chapter 3 will provide a more detailed discussion of the mathematics and methodology behind both the non-collinear wave mixing strategy and the pulse inversion improvement.

Chapter 4 will summarize the experimental preparations and procedures for non-collinear wave mixing, tensile testing, and taking microscopic images.

Chapter 5 will display the results of the nonlinear ultrasonic interrogation, tensile testing, and microscopy images.

Chapter 6 provides conclusions about the studies performed.

Chapter 7 will provide recommendations for future work and will suggest alternative configurations for nonlinear interrogation of HTHA damaged steel.

CHAPTER 2

LITERATURE REVIEW

2.1 Hydrogen Damage in Steels

The effect of hydrogen diffusion into metals has been known since 1875 where it was first discovered by W.H. Johnson. Johnson dipped various metals into acids which evolve hydrogen by their action on iron. Johnson noted that the degree of absorption of hydrogen in metals resulted in increased brittleness [13]. Despite the early identification of the embrittlement effect of hydrogen on steels, the issues surrounding hydrogen embrittlement still remain relevant today. It was soon concluded that hydrogen embrittlement is caused by the diffusion of individual hydrogen atoms on the outside surface of metals. Hydrogen can fuse with other hydrogen damaged areas causing bubbles of hydrogen to remain in the metals. The remaining hydrogen can cause a decrease in strength and ductility [14]. Studies continue focused mainly on the prevention of hydrogen embrittlement and identifying environments and conditions in which it may occur [15]. However, in addition to the issues with hydrogen embrittlement, it was later noticed that hydrogen can cause further issues while under high temperature high pressure conditions. This problem originated from hydrogen interacting with an alloying or impurity elements in the microstructure of a metal. This exacerbation of the hydrogen diffusion problem was deemed high temperature hydrogen attack.

Hydrogen attack has been studied as early as 1919 where high temperature hydrogen decarburization was examined by Campbell [16]. Studies continue to this day, exploring the effects of various combinations of pressures, temperatures, and alloyed steels. The most insightful work on hydrogen attack of steel was conducted in depth by Paul Shewmon in

1976 [17]. Shewmon noted that steels operating with exposure to high partial pressures of hydrogen and high temperatures can operate for days or months and then suddenly and rapidly lose ductility and strength. This is due to the nucleation, growth, and coalescence of methane bubbles along grain boundaries within carbon steels. This type of damage, distinct from hydrogen embrittlement, is HTHA. The chemical process by which these methane bubbles form is shown below:

$$8H + C + Fe_3C = 2CH_4 + 3Fe \tag{2.1}$$

This Equation describes the movement of hydrogen into the steel, followed by the merging of hydrogen and carbon to form methane, and finally the movement of iron away from the newly formed methane. As the carbon combines with hydrogen, the carbon is lost from the steel in a process called decarburization, or the loss of carbides from the metal. Additionally, methane cannot diffuse out of steel, forming methane bubbles. These bubbles then combine resulting in localized micro-fissures with a characteristic length of 1 μm. If the damage continues to progress, these fissures can also combine to form cracks on the scale of 0.1 to 1.0 mm. These cracks are often seen along grain boundaries and along inclusions in the rolling direction of the steel [18]. Note that rolling is a manufacturing process that shapes steel for a particular task. The formation of fissures and cracks and the decarburization of steel, all resulting from HTHA, contribute to the loss of strength in a pressure vessel.

Pressure vessels subject to conditions in which HTHA is possible, can operate normally for a significant amount of time prior to the initiation of HTHA. Due to this, at early times during the HTHA damage process, the concentration of hydrogen is localized only near the inside surface of the pressure vessel, where the steel is exposed to the hydrogen. Later, once the hydrogen diffuses further into the steel, a linear hydrogen concentration gradient may be established [17]. Methane begins to form after some incubation time, where the hydrogen concentration increases to initiate the process. Due to this incubation time, the exposure of the inside surface of a pressure vessel is prolonged and HTHA damage initiates

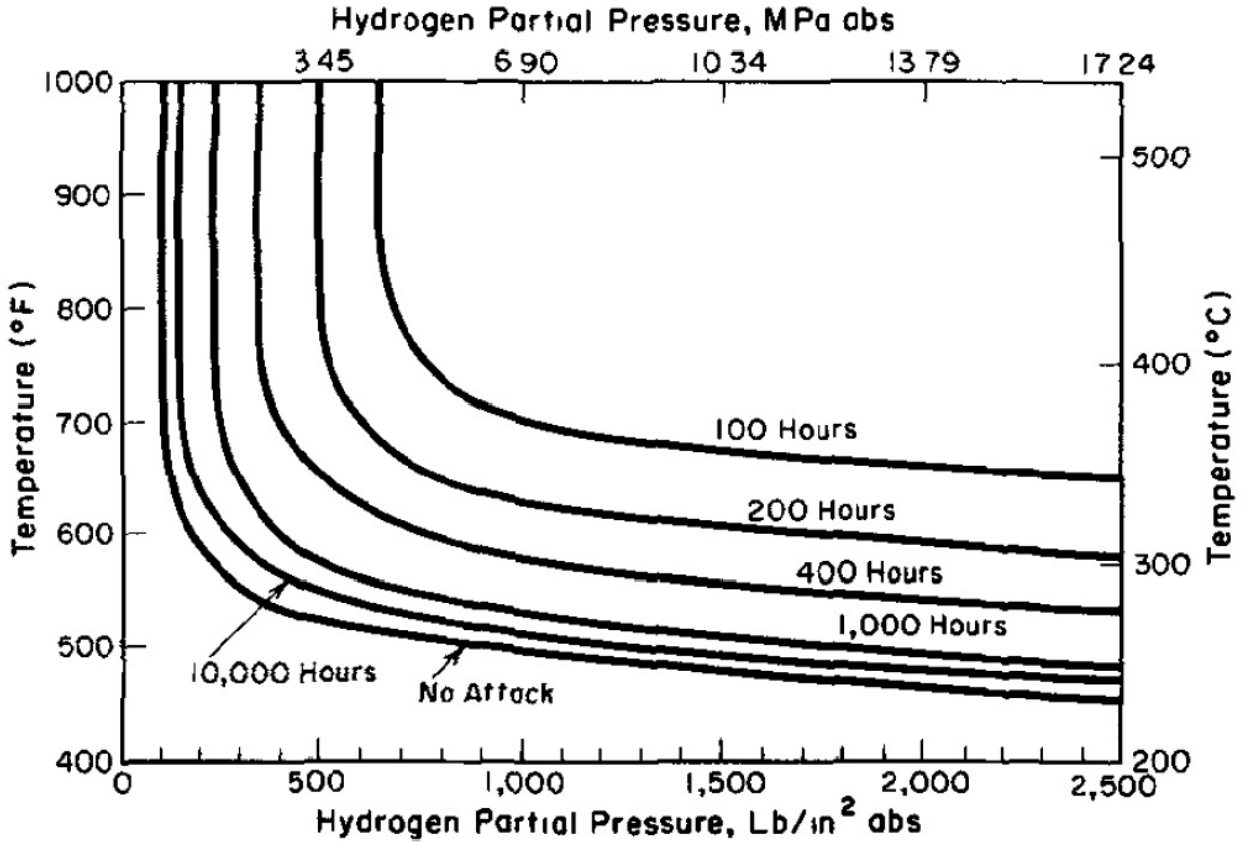

Figure 2.1: Illustration of an API 941 Nelson Curve, showing two different steel types. Extracted from [4, 5]

first at this surface. As a result, the amount of damage is greatly increased near the inside surface as the process continues. The accumulation of damage closer to the inside surface causes a nonlinear distribution of HTHA damage throughout the thickness of a specimen. HTHA can begin near the inside surface prior to the nucleation of methane at further distances from the surface [17]. As previously mentioned, efforts have been made to reduce the prevalence of this type of damage. The most widely accepted design measure for creating steel pressure vessels comes in the form of Nelson Curves [5]. These curves plot the operating conditions, or the hydrogen partial pressure versus temperature, in which various steels can be safely used. The curves represent the limits of safe operation for a particular type of steel. Nelson Curves are sufficient when the vessels are operated well within the specified temperature and pressure limits; however, in real operating conditions, these limits are often surpassed. Surpassing these limits can occur during maintenance,

shutdown, and start-up conditions. Additionally, because nelson curves were created with accumulated data, operating a pressure vessel just below the nelson curve is not a guarantee that HTHA will not occur [19].

2.2 HTHA Detection

2.2.1 Microscopy

Traditionally, the most definitive way to detect the presence of HTHA is by using microscopy or metallography techniques on previously damaged steel. Microscopy, in this case, is the process of grinding, polishing, and etching a steel surface in order to examine the microstructure under a microscope. By doing this, small fissures and cracks caused by HTHA become visible, allowing for the verification of damage. These techniques are effective in identifying HTHA but they have significant draw backs. For example, in an operational pressure vessel, only the outside surface of the specimen is accessible for examination, but it is the least likely area to be damaged. Microscopy only allows for inspection of localized areas of a pressure vessel. Additionally, microscopy does not reveal any information about areas deeper in a specimen. Because of this, microscopy is not the most practical form of inspection for detecting HTHA [2].

2.2.2 Linear Ultrasonic Methods

Linear ultrasonic methods have arisen in an attempt to detect HTHA. Traditional linear ultrasonic methods rely on the transmission and reflection of sound waves. In many cases this is useful for detecting large cracks and voids that are of similar length to the inspection wavelength [6]. Though this is useful for many nondestructive evaluation efforts, this basic procedure falls short when trying to inspect for HTHA damage because typical inspection frequencies result in an inspection wave length that is often much too large to reflect off of small HTHA fissures. Due to this issue, some unique methods have developed in an attempt to detect HTHA using these methods and creative analysis. One linear

method that has been considered is the velocity method [20]. The method claims that the speed of sound for either longitudinal or shear waves decreases if HTHA is present. Further, the ratio of shear wave velocity to longitudinal wave velocity increases with HTHA damage. Though this method has shown promise, it is important to note that other parameters can affect the velocity response in linear ultrasonics. Additionally, these effects are more likely to occur with increased travel distance [21]. As a result, this particular method has been shown to produce false positives for HTHA damage and produces unreliable results. Therefore, this method is almost exclusively recommended to be used in conjunction with other inspection methods [20, 10].

Attenuation has also been proposed as a method of HTHA detection. Attenuation has been shown to increase with HTHA damage [20, 10]. As HTHA inclusions become more prevalent, there is an increase in the scattering attenuation of sound waves. This method relies on using shear wave pulse echo measurements to detect the drop in amplitude that results when measuring specimens with significant HTHA damage, i.e. more HTHA damage will result in smaller reflection amplitudes when compared with non-damaged materials. This is certainly an effect of HTHA damage and is something that must be accounted for even in the most advanced methods of inspection. However, the problems with this method remain. First, straight attenuation measurements through the thickness of a specimen do not account for the variability in damage throughout the thickness and cannot reliably account for the degree of damage in a specimen. Additionally, the attenuation method is influenced by many other factors including corrosion, surface roughness, and transducer coupling which can further increase uncertainty in this method [20]. Because of these issues, the attenuation method cannot stand alone as an inspection technique. However, it is still important to collect attenuation measurements for more advanced inspection methods.

2.2.3 Backscatter

Backscattering amplitude techniques are claimed to have the ability to reliably detect HTHA. Backscattering is a technique in which transducers set-up in a pulse-echo configuration can compare signals between damaged and undamaged steels for damage assessment. When backscattering occurs, a noisy response will reflect back to the transducer prior to the expected arrival time of the back wall echo. By analyzing these early reflections, backscattering techniques utilize an attenuation effect of HTHA by assuming that fissures will increase the amount of scattering, and therefore, increase the amplitude of backscatter signals while measuring HTHA affected materials [22]. The backscattering of sound waves in a HTHA damaged material is also affected by many things including, grain size and inclusion content in addition to HTHA [23]. As a result, early on, these methods could not differentiate HTHA damage from other parameters such as grain size, inclusions, and surface geometry. As research continued, it was noted by W. D. Wang [22] that by comparing signals from a non-damaged HTHA effected region and a damaged HTHA region of the same material HTHA can be identified. This process involved deconvolution of the damaged signals by removing the effects of parameters present in the non-damaged signals. Despite advances in this method, the strategy proves to be difficult. Backscatter methods have shown to have some effectiveness in terms of verification of the presence of damage, but they are not reliable for scanning entire specimens. A binary verification is not ideal when there is a strong need for scanning capabilities. The risk of falsely identifying HTHA damage is also present when using this technique because inclusions can cause similar signal characteristics to HTHA and inclusions near an inner diameter of a specimen can result in false positives [24]. This also shows that the use of these techniques would require a technician with substantial understanding of the mechanisms of HTHA damage in order to positively and reliably diagnose HTHA damage. Since these methods have the aforementioned issues, they are not reliable and not suitable for large scale scanning [5, 10]. There remains a need for a method which can handle more in-depth analysis of pressure vessels.

2.3 Non-Collinear Wave Mixing

Development of the techniques involved in nonlinear ultrasonic testing date back to the early 1950s where third-order nonlinear Equations of motion were first being developed by Murnaghan [25]. Further advancements in the 1950s led to the development of third order elastic constants which were first experimentally measured in 1953 using ultrasonic sound velocities [26]. The first consideration of 1-dimensional propagation of waves and self-interaction effects were made by Goldberg in 1960. The first experimental observations of nonlinear interactions of collinear bulk dilatational waves was made by Shiren [27] in 1963. He was able to indirectly prove the existence of nonlinearities in an acoustic signal. A nonlinear wave was first directly detected by Rollins in 1963. He observed scattered waves in aluminum and magnesium for multiple interaction cases proposed by Jones and Kobett [28, 29]. With verifications of these nonlinear interactions, it was proposed that these interactions could be used to predict third order elastic constants. In 1967, Krasilnikov and Zarembo [30] presented results from an experiment testing wave interactions in solids. They were able to observe a nonlinear scattered wave that resulted from primary wave interaction. They were additionally able to verify the observed nonlinear scattered wave was a result of the wave interaction and not from the system configuration. They did this by studying the time domain record when both transducers were operated simultaneously and individually, showing that the scatted wave was only present when both transducers operated together. This method of verification became an important aspect in nonlinear ultrasonic experiments.

The 1970s saw a decrease in the number of publications focused on nonlinear ultrasonics but there was a significant study conducted in 1973 by Hiki and Mukai [31]. By studying wave interactions in copper, they were able to verify the existence of scattered nonlinear waves in two separate interaction cases. More importantly, Hiki and Mukai were able to show that the amplitude of the nonlinear wave was proportional to the volume of interaction and the product of the amplitudes of the primary waves. This is an essential component to modern nonlinear ultrasonic testing, since the effects of the nonlinear

amplitude must be well known in order to properly use these methods. The next major improvement to the theory of nonlinear acoustics came in 1987, when Nazarov [12] began to consider nonlinear acoustics in micro-inhomogeneous materials. Micro-inhomogeneous materials are materials with small cracks and dislocations which are small relative to the wavelength of a propagating wave, much like what is seen in HTHA damaged steel. In that study, it was concluded that the presence of small inhomogeneities in a medium enhances the nonlinear response. In two studies conducted in 1987 and 1989, Johnson and Shankland illustrated that non-collinear wave mixing was possible in rock due to the presence of micro cracks which cause nonlinearity within the material [32, 33]. Additionally, they introduced a set of criteria that ensured the scattered wave originated from the primary waves interacting with one another and not from the testing system. These three criteria are (1) the nonlinear scattered wave (in this case) must be the difference frequency (difference between the two primary wave frequencies, (2) the amplitude of the nonlinear scattered wave must be proportional to the product of the amplitudes of the primary beams, and (3) the trajectory and frequency ratios of the nonlinear generated signal must match those predicted by theory. These criteria are typical for nonlinear interrogation of materials.

Many more publications were created in the 1990s that extended theories to better accommodate real world applications. However the next relevant piece of work was conducted by Korneev in 1998 [34], where an in-depth report on nonlinear ultrasonic wave mixing can be found. Korneev's work includes amplitude expressions for all possible interaction cases. Further improvements were made to the work done by Korneev by himself and Demcenko in 2013 [35]. Using non-collinear wave mixing for the detection of material degradation was first proposed by Croxford in 2009 [36]. This method was applied to aluminum samples which underwent varying degrees of fatigue or plastic deformation. This method relied on measuring the amplitude of the scattered wave and then normalizing it by the amplitudes of the two primary waves. The normalized amplitude measurements was termed the normalized nonlinearity parameter. In this study, the authors were able to show that with increased levels of fatigue/plasticity the normalized nonlinear parameter increased as well. This same method was again applied by Demcenko

and others in order to measure the levels of aging in PVC, thermoplastics and cured epoxy [37]. In 2016, non-collinear wave mixing was successfully used by McGovern [1] to measure the degree of high temperature hydrogen attack in a steel pressure vessel using an approach very similar to those used by Croxford and Demcenko. This paper completed by McGovern is closely related with the work that will be presented in the following sections; further details from this work will be discussed as well.

CHAPTER 3

METHODOLOGY

3.1 Non-Collinear Wave Mixing

As mentioned previously, there is a significant difference between linear ultrasonics and nonlinear ultrasonics. In a linear elastic medium, two monochromatic waves propagating towards each other will cross paths and the resultant wave in the volume of intersection is simply the superposition of the intersecting waves. However, in a nonlinear elastic medium, assuming the correct conditions are met, the two intersecting waves can intersect and create a third wave. Nonlinear ultrasonic methods take advantage of this phenomenon. There are various combinations of possible nonlinear interaction cases for nonlinear interrogation. Out of 54 possible interaction cases, 8 cases satisfy the necessary conditions able to produce a nonlinear scattered wave. For the interaction cases which are valid, the interaction between primary waves must satisfy both polarization conditions and resonance conditions as described by Korneev [34]. For the purposes of this study, only one particular case is used. In the remainder of this section, this case will be described in more detail.

Consider Figure 3.1; in this figure, k_1 and k_2 represent the primary wave vectors while k_3 represents the scattered wave vector. The primary waves collide to produce the scattered wave; primary and scattered waves should not be confused. Each wave will propagate with a particular frequency which is commonly denoted with ω. The values ω_1, ω_2, and ω_3 are the angular frequencies of the two primary waves and the scattered wave, respectively. The first necessary condition for interactions to occur is the scattered wave angular frequency and the scattered wave vector must be a sum or difference between the two primary waves.

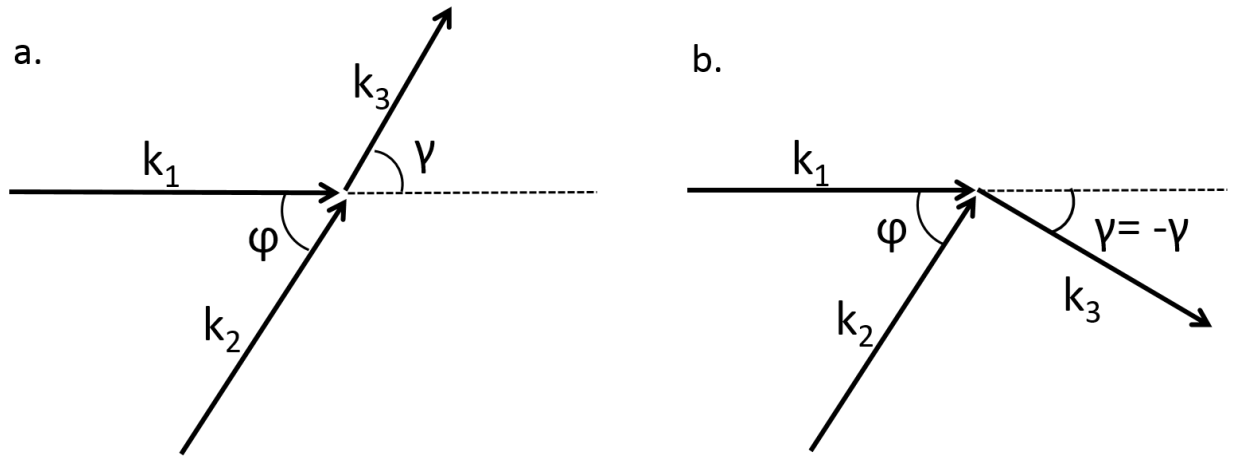

Figure 3.1: Simple representation of intersecting waves, case a represents a non-collinear collision that results in a sum frequency. Case b represents a non-collinear interaction with a difference frequency.

This is represented by the Equations below:

$$\omega_3 = \omega_1 \pm \omega_2 \tag{3.1}$$

$$k_3 = k_1 \pm k_2 \tag{3.2}$$

The particular case used for this study is a case which results in a scattered wave of a sum frequency (i.e. the scattered wave frequency is the sum of the primary wave frequencies). This corresponds to Figure 3.1 part a. The angle of the scattered wave with respect to the k_1 primary wave is counter clockwise. In addition to the conditions shown in Equations 3.1 and 3.2, nonlinear interactions must also satisfy resonance and polarization conditions. These conditions are often the most difficult to satisfy. This is the reason only a select few (i.e. 8 out of 54 cases) can actually produce nonlinear scattered waves.

Resonance conditions are satisfied when the when the expression for the displacement of the scattered wave is constant in a particular direction, for a particular mode (longitudinal or shear), with a sum or difference frequency. This occurs when the volume factor for a particular non-collinear case results in a scattered wave that is directly proportional to the size of the interaction region and the scattered wave amplitude does not oscillate [35, 38].

For the sake of brevity, only the case that is used in this study will be discussed[1]. The resonance condition which describes the non-collinear interaction between two shear waves to produce a longitudinal wave, as shown by McGovern [38], is shown in Equation 3.3.

$$\frac{\omega_1 + \omega_2}{c_L} r_s - (k_1 + k_2) = 0 \tag{3.3}$$

Where ω_1 and ω_2 are the primary wave frequencies, c_L is the scattered wave speed, and r_s is the unit vector which corresponds to a direction pointing from the center of the interaction point to the observation point. Additionally, the angles at which the primary waves interact, denoted φ, as seen in Equation 3.1, must fall within the following range described by Equation 3.4, this is because the waves are non-collinear in this case:

$$-1 < \cos\varphi < 1 \tag{3.4}$$

The angle denoted γ in Figure 3.1 represents the direction in which the scattered wave travels with respect to the k_1 direction. Some helpful geometric relationships which result from the interaction shown in Figure 3.1 are shown below in Equations 3.5 and 3.6.

$$k_1 \cdot k_2 = k_1 k_2 \cos\varphi \tag{3.5}$$

Also, from Figure 3.1 part a, using relationships from the sum frequency case, the following progression can be made:

$$\begin{aligned} k_3 &= k_1 + k_2 \\ k_3^2 &= k_1^2 + k_2^2 + 2k_1k_2\cos\varphi \\ k_2^2 &= k_1^2 + k_3^2 - 2k_1k_3\cos\gamma \\ \cos\gamma &= \frac{k_1 + k_2\cos\varphi}{k_3} \\ \sin\gamma &= \frac{k_2}{k_3}\sin\varphi \end{aligned} \tag{3.6}$$

[1]For a complete overview on non-collinear wave mixing please see the appendix of reference [38].

It is also important to note that the wave number k is simply the ratio of angular frequency to wave speed, ($k = \omega/c$). Using this and the relationship shown in Equation 3.5, Equation 3.7 shows the following useful relationship:

$$k_1 \cdot k_2 = \frac{\omega_1 \omega_2}{c_s^2} \cos\varphi \tag{3.7}$$

Finally, equation 3.3, which corresponds to the resonance condition for two shear waves interacting to form a longitudinal wave, is squared leading to the progression shown below.

$$\begin{aligned} \left[\frac{\omega_1 + \omega_2}{c_L}\right]^2 r_s^2 &= (k_1 + k_2)^2 \\ \left[\frac{\omega_1 + \omega_2}{c_L}\right]^2 &= k_1^2 + k_2^2 + 2k_1 k_2 \cos\varphi \\ \left[\frac{\omega_1 + \omega_2}{c_L}\right]^2 &= \left(\frac{\omega_1}{c_s}\right)^2 + \left(\frac{\omega_2}{c_s}\right)^2 + 2\left(\frac{\omega_1}{c_s}\right)\left(\frac{\omega_2}{c_s}\right)\cos\varphi \end{aligned} \tag{3.8}$$

With further manipulation using the relationships shown in Equations 3.7 and 3.6, the following expressions for $\cos\phi$ and $\tan\gamma$ are reached.

$$\cos\varphi = \left(\frac{c_S^2}{c_L^2}\right) + \frac{1}{2}\left(\frac{\omega_1}{\omega_2} + \frac{\omega_2}{\omega_1}\right)\left(\frac{c_S^2}{c_L^2} - 1\right) \tag{3.9}$$

$$\tan\gamma = \frac{\sin\gamma}{\cos\gamma} = \frac{k_2 \sin\varphi}{k_1 + k_2\cos\varphi} \rightarrow \tan\gamma = \frac{\omega_2 \sin\varphi}{\omega_1 + \omega_2 \cos\varphi} \tag{3.10}$$

c_L and c_S are the longitudinal and shear wave velocities, respectively, φ is the angle between the two primary waves k_1 and k_2, and γ is the angle between the k_1 primary wave and the scattered wave k_3. If these Equations are satisfied for this particular configuration, then resonance conditions are also satisfied. Because resonance conditions are satisfied, an interaction may be possible assuming polarization conditions are met as well. Note from the requirements, ω_2 is less than or equal to ω_1 (by definition), c_S is less than c_L (material property), and the relationship shown in Equation 3.4 is the geometric criteria for

non-collinear wave mixing. The three parameters, φ , γ, and the ratio $\frac{\omega_1}{\omega_2}$ are interrelated, such that when one is chosen then the other two are fixed.

Polarization conditions must also be satisfied in order for a nonlinear interaction to occur. Amplitude calculations have been carried out in the past and covered in detail by Korneev [35]. Depending on the conditions of a nonlinear interaction, the scattered wave amplitude could be zero. When this occurs, even if resonance conditions are met, the polarization conditions are not satisfied and no interaction occurs. For this study, the case where two shear waves interact to produce a sum frequency longitudinal wave is used. Up until this point, nothing has been mentioned about the polarization of the primary shear waves in this experiment. Based on conclusions from Korneev [35], as long as both primary shear waves are polarized in the same direction, i.e. polarized in the k_1-k_2 plane or out of the k_1-k_2 plane, polarization conditions are satisfied and an interaction will occur. In this study, longitudinal transducers are placed on wedges and shear waves are induced in the test specimen, this results in primary shear waves that are polarized in the k_1-k_2 interaction plane. Therefore, polarization conditions are met and the interaction is possible. It is worth noting that if the two primary shear waves did not have the same polarization, the interaction would not occur.

3.1.1 Non-collinear Wave Mixing For Nonlinear Interrogation

Consider the case described above where two monochromatic waves, in this case shear waves, are propagated such that they eventually cross paths for non-collinear interaction. The displacement amplitudes of these two primary waves as they travel can be written as follows:

$$y_1(r,t) = A_1 \sin\left(k_1 \cdot r - \omega_1 t + \phi_1\right) \tag{3.11}$$

$$y_2(r,t) = A_2 \sin\left(k_2 \cdot r - \omega_2 t + \phi_2\right) \tag{3.12}$$

Where A is the amplitude, k is the wave vector, r is the displacement vector, ω is the angular frequency, t is time, and ϕ is the phase. The subscripts 1 and 2 denote the first and second primary wave, respectively. If the two waves interact to produce a third scattered wave, its amplitude can be written simply as follows:

$$y_3(r,t) = \beta(x)A_1A_2 \sin\left[(k_1 \pm k_2)\cdot r - (\omega_1 \pm \omega_2)t + \phi_3\right] \tag{3.13}$$

Where $\beta(x)$ is the efficiency of the interaction between primary waves, or the fraction of energy converted from the primary waves into the nonlinear scattered wave. Notice that the frequency of the nonlinear scattered wave is either the sum or difference frequency $\omega_1 \pm \omega_2$ of the two primary waves. For this study, the scattered wave has a sum frequency. Also note that the primary waves are polarized in the plane of interaction.

3.2 Pulse Inversion

To improve signal-to-noise ratio, the pulse inversion technique can be used. This technique relies on the fact that a 180° phase shift in the primary waves will correspond to a 360° or 0° phase shift in the nonlinear scattered wave for sum and difference waves, respectively. The pulse inversion technique is often implemented in harmonic generation applications [11] and has also been implemented in collinear wave-mixing applications [39]. However, it has yet to be implemented in non-collinear wave-mixing. In addition to filtering the data, the pulse inversion technique has the potential to improve quality of the received scattered wave signal.

Recall the amplitude expressions for the two primary waves and corresponding nonlinear scattered wave as written in Equations 3.11 through 3.13. At nodes, points of zero amplitude, the sine argument is zero and expressions for the primary wave phases can be expressed as:

$$\phi_1 = \omega_1 t - k_1 \cdot r \tag{3.14}$$

$$\phi_2 = \omega_2 t - k_2 \cdot r \tag{3.15}$$

Similarly for the nonlinear scattered wave:

$$\phi_3 = (\omega_1 \pm \omega_2)t - (k_1 + k_2) \cdot r \tag{3.16}$$

From the expressions in Equations 3.14 and 3.15, the phase of the nonlinear scattered wave is equivalent to:

$$\phi_3 = \phi_1 \pm \phi_2 \tag{3.17}$$

This can be expressed in terms of the phase difference or shift as follows:

$$\Delta\phi_3 = (\Delta\phi_1 + \Delta\phi_2) \tag{3.18}$$

Thus, for a 180° phase shift for the primary waves:

$$\therefore \Delta\phi_3 = \begin{cases} 0^\circ & \text{difference frequency} \\ 360^\circ & \text{sum frequency} \end{cases} \tag{3.19}$$

A 180° phase difference corresponds to an out-of-phase wave, whereas 0° and 360° are in-phase. As a result, when the primary waves are first sent with no phase shift, and then sent with a 180° phase shift, the summation of these two signals will result in the cancellation of the primary waves and constructive interference in the scattered wave. With this knowledge, the data collection scheme would be as follows: 1) collect time record of interaction between two primary waves, 2) invert pulses of two primary waves and collect time record, 3) add records from steps 1 and 2. The resulting signal from step 3 would ideally consist of only the nonlinear scattered wave. Also note that since the phase difference of the nonlinear wave results in constructive interference, the measured nonlinear signal after step 3 has twice the amplitude than what it would have had without pulse inversion. This is one of the main advantages to this method. Increasing the amplitude of the nonlinear signal increases the signal to noise ratio and the nonlinear response is more easily identifiable. Also note that in previous studies which utilized non-collinear wave mixing, the data collection technique required operating both primary wave signals

simultaneously, and then operating each primary wave transducer individually and recording the time records of all three. Then, the sum of the individual signals is subtracted from the simultaneous signal. This process is effective, but more tedious than using pulse inversion because more data collection and processing is required.

3.3 Nonlinear Parameter

The amplitude of the nonlinear scattered wave represented in Equation 3.13 is proportional to the product of the two primary waves (k_1 and k_2), the volume of interaction, and the efficiency of interaction. To account for all of these factors, the simplified nonlinear wave amplitude is represented by Equation 3.20.

$$A_3(x) = 2\beta(x)A_1A_2e^{-\alpha_L(x)d_{NL}(x)}e^{-2\alpha_s(x)d_p(x)} \tag{3.20}$$

$\beta(x)$ represents the efficiency of the interaction between the primary waves and d_{NL} and d_P are propagation paths of the nonlinear scattered wave and the primary waves respectively. α_L and α_S are the longitudinal and shear attenuation coefficients (Np/m) respectively. A_1, A_2 and A_3 are the amplitudes of the primary waves and scattered waves respectively. The variable x represents the distance (m) from the interaction region to the outside surface of the test piece. Note that Equation 3.20 represents the amplitude of the nonlinear wave after using the pulse inversion technique. Again, because the nonlinear amplitude is measured using the pulse inversion technique, the nonlinear amplitude after data processing is doubled. This is due to constructive interference in the scattered wave and cancellation in the primary waves. Because $\beta(x)$ represents the efficiency of interaction and is proportional to the degree of nonlinearity [12], the next step is to solve for $\beta(x)$.

$$\beta(x) = \frac{A_3(x)}{2A_1A_2e^{-\alpha_L(x)d_{NL}(x)}e^{-2\alpha_s(x)d_p(x)}} \tag{3.21}$$

In order to compare β parameters across the thickness of the specimen, it is necessary to normalize these values with the material layer closest to the outside surface. This

normalization yields Equation 3.22.

$$\frac{\beta(x)}{\beta(0)} = \frac{A_3(x)}{A_3(0)} \left(\frac{e^{-\alpha_L(0) d_{NL}(0)} e^{-2\alpha_s(0) d_p(0)}}{e^{-\alpha_L(x) d_{NL}(x)} e^{-2\alpha_s(x) d_p(x)}} \right) \tag{3.22}$$

Note that in some cases, including the case utilized in this study, $\beta(0) = 0$. When this is the case, a $\beta(x)$ value corresponding to a material layer closer to the inside surface can be used as the normalization parameter. A $\beta(x)$ value corresponding to a depth of 0.1 cm from the outside surface was used as a normalization parameter for this study.

The normalized parameter, $\beta(x)/\beta(0)$, is an indicator of the amount of damage within the specimen. Accurate measurements of the nonlinear scattered wave are necessary to obtain a damage profile in a test specimen. Equation 3.22 shows that attenuations will have an effect on the estimates of the $\beta(x)/\beta(0)$ parameter. In section 4.1, measuring and estimating attenuation will be described in more detail.

CHAPTER 4

EXPERIMENTAL PREPARATION AND PROCEDURES

4.1 Linear Acoustic Characterization

A test sample procured from a retired pressure vessel with severe HTHA damage was obtained from a refinery. The test sample has a nominal thickness of 30 mm and has severe cracking through the center of the specimen, as can be seen in Figure 4.1. The large crack can be attributed to inhomogeneities along the location of the crack, making this portion of the specimen more susceptible to HTHA damage. The increased fissuring sensitivity in certain areas can arise from inclusions or a uniform boundary layer [40]. Inhomogeneities can cause complete separation of grains during the HTHA process and exasperate fissuring. It is therefore necessary to probe the specimen for areas that do not have significant cracking. This can be done by verifying that pulse-echo measurements are traversing the entire specimen. As can be seen in Figure 4.1, a large area on the lower left hand side has been polished. This area was chosen for nonlinear interrogation because signals were found to traverse the entire specimen thickness mostly undisturbed. Note that polishing the surface improves couplant conditions and allows for more consistent testing results. From

Figure 4.1: Bare test specimen, showing large cracks running through the center.

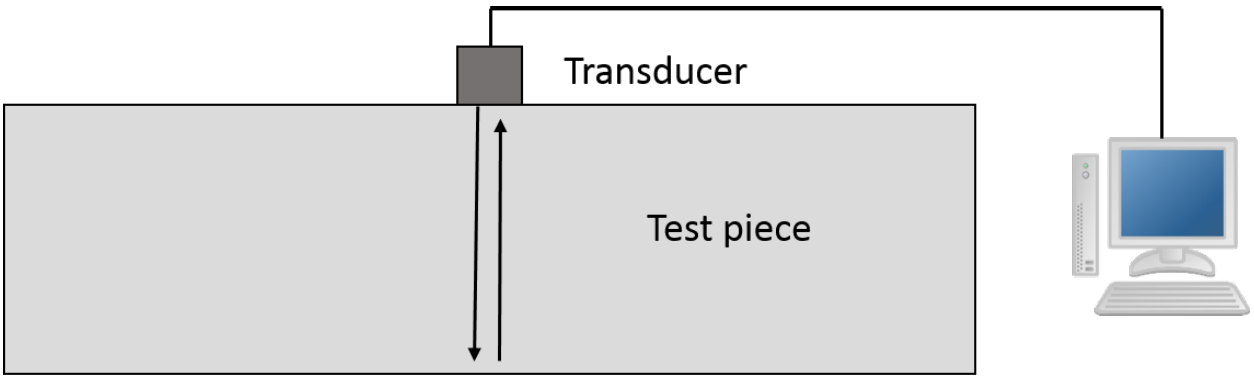

Figure 4.2: Typical set up for single transducer pulse-echo probing.

here, linear characterization can begin.

As mentioned in section 3.3, in order to fully analyze nonlinear ultrasonic measurements, linear ultrasonic parameters must be measured. In this case, the test specimen has been previously analyzed by McGovern. Both velocity data and attenuation data have been borrowed with permission from the authors [1]. An important objective of this study is to show that single sided linear and nonlinear interrogation is possible for HTHA damage. To maintain this theme, measurement techniques will be primarily constrained single sided surface measurements.

4.1.1 Average Velocities and Attenuations

The first method utilized for linear probing of the specimen was to make simple pulse-echo measurements. Pulse-echo measurement relies on sending and receiving pulses with a single transducer and analyzing the resulting reflections. A schematic of this type of measurement can be seen in Figure 4.2. These measurements can provide the average velocity and attenuation of both longitudinal and shear waves over the thickness of the specimen. Velocities can be measured by comparing the main bang signal to reflection signals that correspond to the back wall echo. Velocities have been verified further with a phase comparison method for velocity measurement [41]. For each wave mode, frequencies

[1]Linear characterization values for the testing specimen were utilized with permission from the author [1].

corresponding to the non-collinear wave mixing method were used. Shear waves were operated at a center frequency of 3.5 MHz, while longitudinal waves were operated at 7 MHz. This is due to the fact that during non-collinear wave mixing, the primary waves will be interacting to form a sum frequency longitudinal scattered wave, i.e. $f_1 + f_2 = f_3$ where f_1 and f_2 are chosen to be 3.5 MHz. Note that although linear acoustic measurements are not sensitive enough to detect HTHA, they are still necessary for nonlinear characterization since time of flight estimates and attenuation coefficients are needed to correctly identify and measure nonlinear waves. Results determined by McGovern from pulse-echo measurements can be found in Table 4.1. They are listed as the mean velocities and the mean attenuation values.

4.1.2 Surface Wave Measurements

The damage within the specimen is not uniform due to increased methane and hydrogen concentration towards the inside surface of the specimen. This causes the level of HTHA damage to vary through the thickness, so in addition to the average attenuations measured through the thickness of the specimen, it is necessary to obtain the attenuation values for the inside and outside surface. These measurements are necessary to have prior to nonlinear characterization. Surface waves can be used to measure the attenuations at the surface of the specimen. For estimation of longitudinal attenuations, critically refracted subsurface longitudinal waves can be employed. These surface waves have the advantage that they travel nearly parallel to the surface of the test piece but still travel as a uniform longitudinal mode [6]. These waves can be generated by using angle wedges to send in waves at the critically refracted angle governed by Snell's law. This relationship is shown below in Equation 4.1.

$$c_{wedge} \sin 90^\circ = c_L \sin \theta_{inc} \tag{4.1}$$

This Equation simply represents Snell's law at the first critical angle. The value c_{wedge} corresponds to the longitudinal velocity in the wedge; c_L corresponds to longitudinal wave velocity; and θ_{crit} is the incident angle of the wedge (i.e. the first critical angle). An

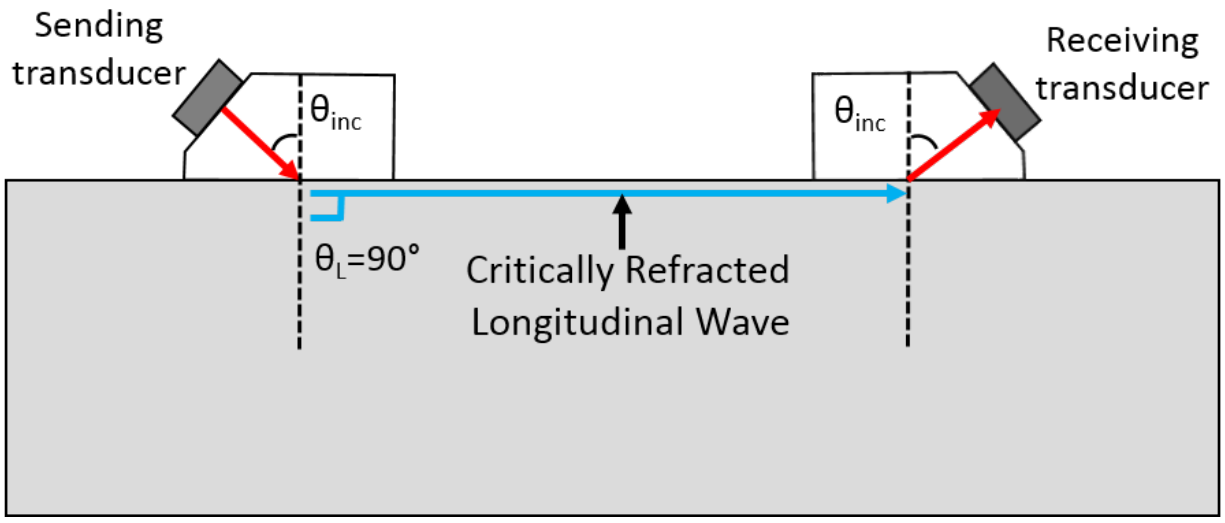

Figure 4.3: Longitudinal subsurface wave measurement configuration. θ_{inc} must be set to the first critical angle governed by Snell's law in order to induce critically refracted waves [6].

illustration of the configuration for this particular measurement technique can be seen in 4.3. This strategy allowed for attenuation on the inside and outside surface to be measured, results can found in Table 4.1 and Figure 4.4.

After longitudinal values are determined, it is necessary to obtain shear attenuation values along the surface of the specimen. In order to estimate these values, Rayleigh surface waves can be employed. Rayleigh waves are a linear combination of longitudinal and shear wave modes. Because longitudinal surface values have been obtained through critically refracted subsurface longitudinal waves, Rayleigh waves can be used to estimate shear attenuation. Much like critically refracted subsurface waves, Rayleigh waves can be induced on the surface of a specimen by using a wedge. In this case, the wedge must be at an angle that makes the Equation 4.2 true:

$$c_{wedge} \sin 90^\circ = c_R \sin \theta_{inc} \tag{4.2}$$

Equation 4.2 is simply Snell's law corresponding to Rayleigh wave induction. Note that c_{wedge} corresponds to the longitudinal velocity in the wedge, c_R corresponds to Rayleigh wave velocity and θ_{inc} is the incident angle of the wedge. Rayleigh wave speed can be

approximated by Equation 4.3.

$$\frac{c_R}{c_S} = \frac{.862 + 1.14v}{1 + v} \tag{4.3}$$

Where c_R is Rayleigh wave speed, c_s is the shear wave speed, and v is Poisson's ratio. This way, if Rayleigh wave speed is not known it can be estimated. Now, if longitudinal attenuation is already known, once Rayleigh waves have been produced and measured, shear attenuations can be estimated. This estimation was accomplished using the process detailed below. This strategy was accomplished using insights from Viktorov [42].

Rayleigh attenuation is related to the shear and longitudinal attenuation through Equation 4.4:

$$\alpha_R \lambda_R = C\alpha_L \lambda_L + (1 - C)\alpha_S \lambda_S \tag{4.4}$$

In this Equation, the parameters are defined as the following values:

$$C = \frac{16\xi^2(1 - \eta^2)}{\eta^2(3\eta^4 - 16\eta^2 - 16\xi^2 + 24)} \tag{4.5}$$

$$\eta = \frac{k_S}{k_R} \approx \frac{.87 + 1.12v}{(1 + v)} \tag{4.6}$$

$$\xi = \frac{k_L}{k_S} = \frac{c_S}{c_L} = \sqrt{\frac{1 - 2v}{2(1 - v)}} \tag{4.7}$$

Here the subscripts R, L, and S represent Rayleigh, longitudinal and shear values, respectively. The value k denotes the wave number (i.e. $k = \omega/c$), v is Poisson's ratio, λ denotes the wavelength, and α represents the respective attenuations in nepers per meter (Np/m). Because these measurements were made on steel, the Poisson's ratio is assumed to be 0.29, which is typical for steel. From the value of Poisson's ratio, the $(1 - C)$ term in Equation 4.4 dominates, allowing the shear attenuation to be approximated by Equation 4.8.

$$\alpha_R \approx \frac{\alpha_R \lambda_R}{(1 - C)\lambda_S} \tag{4.8}$$

Now that the attenuations can be estimated for both shear and longitudinal waves at the surface, comparisons can be made between the mean attenuations through the thickness

and the attenuations found at the surfaces. McGovern verified that the attenuations at the outside surface were lower than the mean attenuations found through the thickness of the specimen [1]. This implies that the attenuation values are larger towards the inside surface. This is expected since HTHA damage is more severe near the inside surface. However, there still remains a problem in determining the attenuation trend through the specimen. Note that in Equation 3.21, the attenuations correspond to a particular depth. It is therefore necessary to account for the variability in attenuation through the thickness.

Through the measurements described above, 3 attenuation coefficients can be measured: (1) at the inside surface, (2) at the outside surface, and (3) the average attenuation through the thickness. These values can be found in Table 4.1. These three values give a suitable baseline to determine a semi-empirical equation detailing the attenuation trend throughout the specimen thickness. Note that access to the inside surface is not possible for in-field inspection, but in a laboratory environment access to this surface allows for measurements that provide verification for the semi-empirical attenuation expression. Development of this expression is briefly described below. This equation and the subsequent results were borrowed with permission from McGovern [1].

Table 4.1: Shear and longitudinal wave velocities and attenuations at the inside surface, outside surface, the mean and the predicted inside surface values calculated from Equation 4.9. Extracted from McGovern [1]

Mean dilitational velocity, c_l (m/s)	Mean Shear velocity, c_s (m/s)	Dilatational Attneuation, α_l (Np/m)				Shear Attneuation, α_s (Np/m)			
		Measured Values			Estimated by emperical equaiton at inside surface	Measured Values			Estimated by emperical equaiton at inside surface
		Outside Surface	Mean	Inside Surface		Outside Surface	Mean	Inside Surface	
5768	3107	29	37	64	61	66	73	93	92

Since the test specimen was subject to extensive HTHA damage over a long period of time, there is a difference in the effect HTHA has on scattering attenuation depending on service time. At early service times, while methane bubbles and microstructure grain sizes are smaller than probing ultrasonic wavelengths, the attenuation due to scattering can be assumed to follow a Rayleigh regime. Rayleigh regime attenuation assumes that the scattering attenuation corresponds to $\alpha_R \propto \varepsilon\omega_0^4 d^3$ where ε is a material constant, ω_0 is the angular frequency, and d is the characteristic microstructural length. As operation time increases, HTHA damage can further progress and fissures increase in size. Once the characteristic lengths of HTHA damage (methane fissures) approach the same magnitude of probing ultrasonic wavelengths, then a stochastic regime can be assumed for scattering attenuation. With this assumption, attenuation corresponds to $\alpha_S \propto \varepsilon\omega^2 d$ [43]. Based on these insights, the following semi-empirical equation was developed by McGovern [1] to estimate the attenuation values throughout the thickness of the specimen.

$$\alpha(x) = \alpha_0 + \frac{4x^3}{t^3}(\alpha_{mean} - \alpha_0) \tag{4.9}$$

In equation 4.9, t represents the thickness of the specimen, x represents the distance from the outside surface, and the two parameters α_0 and α_{mean}, are attenuation values for the outside layer and through the thickness of the specimen, respectively. This equation allows for a simple two parameter (α_0 and α_{mean}) model to be utilized for attenuation estimates. It was also demonstrated by McGovern that the expression is in agreement with the measured attenuations on the inside surface [1] as is shown in Table 4.1. Note that the differences in the predicted attenuation values from Equation 4.9 and measured values were within 5%. The full relationship can be observed in Figure 4.4: displaying the measured values, and corresponding trend lines from Equation 4.9. The important aspect of this model is that all parameters can be measured from the outside surface. Because it is only necessary to access the outside surface, this method could be applied to pressure vessels without access to the inside surface.

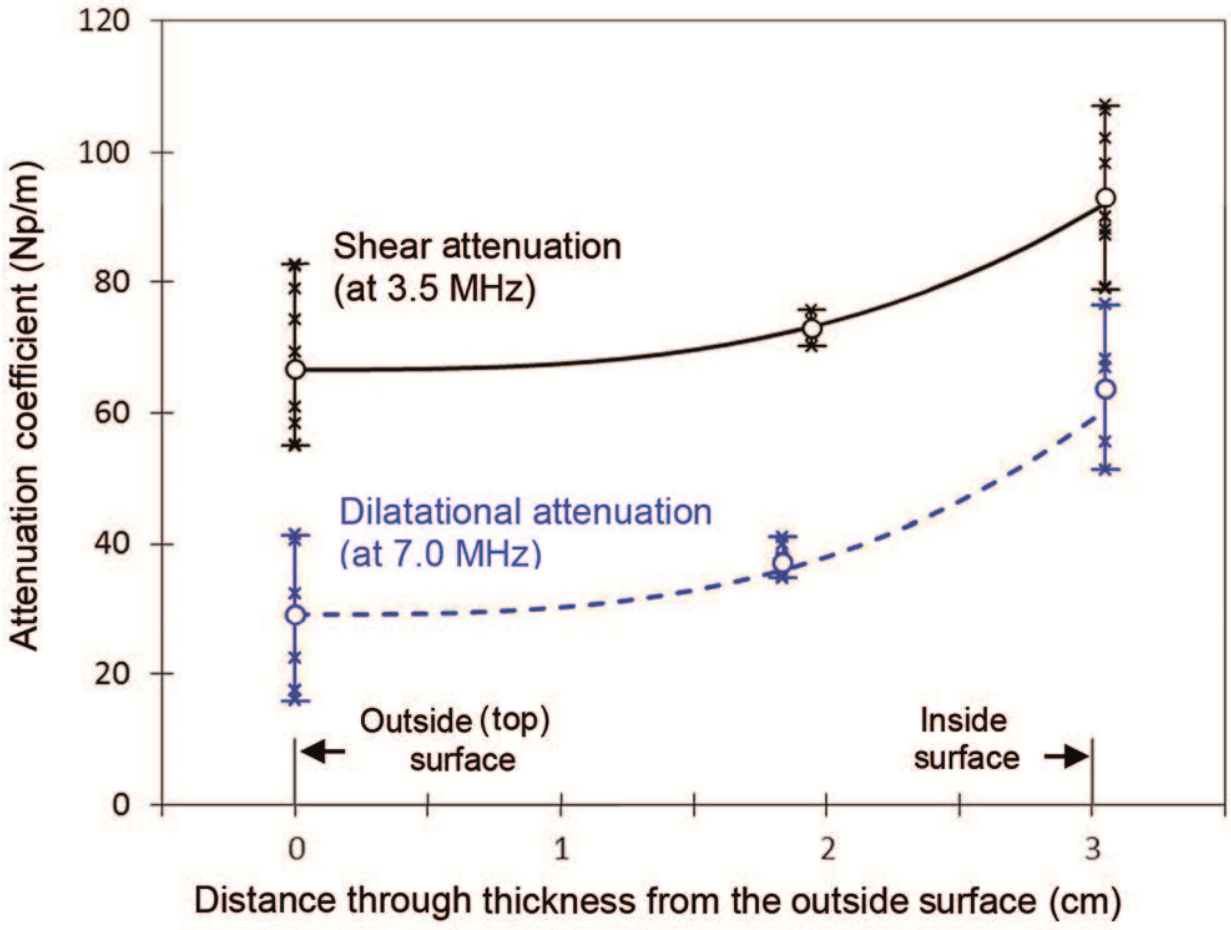

Figure 4.4: Dilatational and shear ultrasonic attenuation coefficients (Np/m) through the thickness of the damaged pressure vessel. Equation 4.9 is plotted as a dashed line is plotted for dilatational attenuation and solid line is plotted for shear attenuation. The Open circles plotted on each curve are the average of ten separate measurements taken at the outside surface, through the thickness, and the inside surface. The error bars correspond to the maximum and minimum values obtained during experimentation. This figure was extracted with permission, from McGovern et al. [1].

4.2 Non-Collinear Wave Mixing Configuration

A configuration first proposed by Croxford [36] was used for this experiment; please see Figure 4.5 for a schematic representation. In this configuration, two longitudinal transducers are mounted on angle wedges to generate refracted shear waves that travel at an angle of 42.7° from the vertical. Angles were determined according to measured shear velocity and Snells law. The two primary wave transducers are 3.5 MHz Olympus A545S-5M. The wedges are Olympus ABSA-5T-45. A pulser-receiver (Ritec RPR-4000) was used to generate a 20 burst sinusoidal wave. The signal from the pulser-receiver was

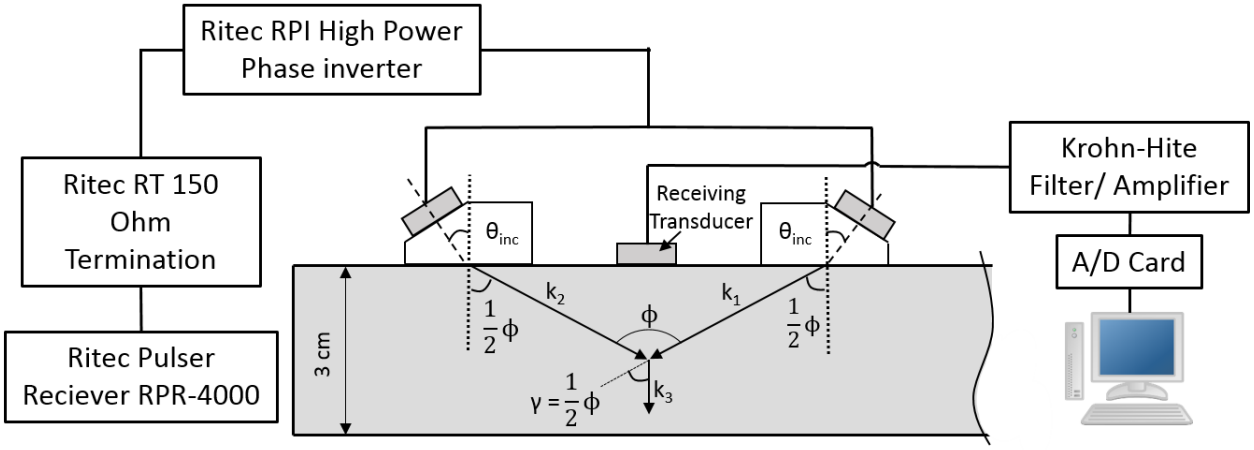

Figure 4.5: Testing configuration schematic diagram for non-collinear wave mixing with a pulse inversion technique.

then split and sent to the primary wave transducers. For each set of tests, the primary waves signals are inverted using the pulse inverter (Ritec High Power Phase Inverting Transformer). An Olympus V121 7.5 MHz center frequency transducer was used as the receiver and was centered between the primary wave wedges on the surface of the test piece. Based on the refracted primary wave angles, the angle ϕ in which the shear waves interact is equal to 85.4°. Because of the symmetry in this testing configuration, the nonlinear scattered wave is propagated in a direction $\gamma = \phi/2$ which reflects perpendicular to the specimen inside surface and travels back through the specimen to directly strike the receiving transducer. Note that this causes the nonlinear wave to travel distance to be larger than the thickness of the specimen. From equations 3.9 and 3.10, in order for the scattered wave to come back directly, the frequencies must be the same, i.e. f_1 must equal f_2. As a result, $f_1 = f_2 = f$ and the interaction between the shear waves results in a sum frequency in the scattered nonlinear wave, $f_3 = 2f$. Therefore during this experiment, the 3.5 MHz primary waves interact to produce a 7 MHz nonlinear scattered wave. One important consequence of this frequency choice is that it is that the nonlinear wave will be at the same frequency as the first harmonics of the primary wave transducers. This negatively affects the frequency separation advantage of non-collinear wave mixing, however, the nonlinear signal can still be identified using time of flight estimates.

Data collection for this experiment was completed in two steps. (1) the primary wave transducers are operated simultaneously and recorded and (2) the primary wave transducers are inverted, operated simultaneously, and recorded. After the records are collected, the two primary wave time-domain signals are summed. The resultant signal should be composed of primarily the nonlinear scattered wave. However, the addition of these signals is not perfect, so a 4th order Butterworth bandpass filter, centered at 7 MHz with a 25 kHz bandwidth, was used to filter out remaining noise. Nonlinear amplitudes were measured from 10 distances spanning 0.1 cm to 2.9 cm in depth from the outside surface. The distance between the primary wave transducers was increased to move the interaction region further from the outside surface of the specimen.

Figure 4.6: Testing configuration, showing both A545S-5M 3.5 MHz primary wave transducers, and the 7.5 MHz Olympus V121 receiving transducer.

Ten different depths were tested through the surface of the specimen by varying the interaction region of the primary waves. The depths measured varied from 0.1 cm and ended at 2.9 cm in depth. There were ten independent measurements for each depth tested. Independence was ensured by recoupling all transducers to the specimen between trials for each depth. Please see Figure 4.6 for the transducer mounted configuration. Interaction depths were predetermined using velocity data and Snell's law. Using the predetermined angles at which the shear waves enter the test piece, the depth of interaction can be adjusted by moving the transducers closer and farther apart. For each depth, transducers were lined up using a straight alignment tool and a pair of digital calipers set to the correct surface distance between transducer wedges corresponding to a

desired interaction depth. Because the receiving transducer was roughly 1/4 inch in diameter, interaction regions close to the outside surface (0.1 cm to 1.25 cm) were measured from the inside surface since the receiving transducer would not fit between the wedges for these distances. However, it is important to note that these measurements could have been made from the outside surface by using a wave guide, though this would require additional measurements of wave guide attenuation, velocity, and transmission and reflection coefficients. In this case, measurements were made from the inside surface because the relevant linear characterization coefficients were already known.

4.3 Tensile Testing

Strength testing has proven to be well correlated with non-collinear damage assessment in previous studies, namely, a study conducted by McGovern which used non-collinear wave mixing and 4-point bending to assess damage in limestone cladding [44]. In order to show a similar correlation, tensile strength tests were completed on machined specimens made from a portion of the same damaged steel pressure vessel. An example of one of the testing specimens can be found in Figure 4.7. Results of the tests will be discussed in Chapter 5, where a comparison between the nonlinear parameter and the reduction in strength through the thickness will be compared.

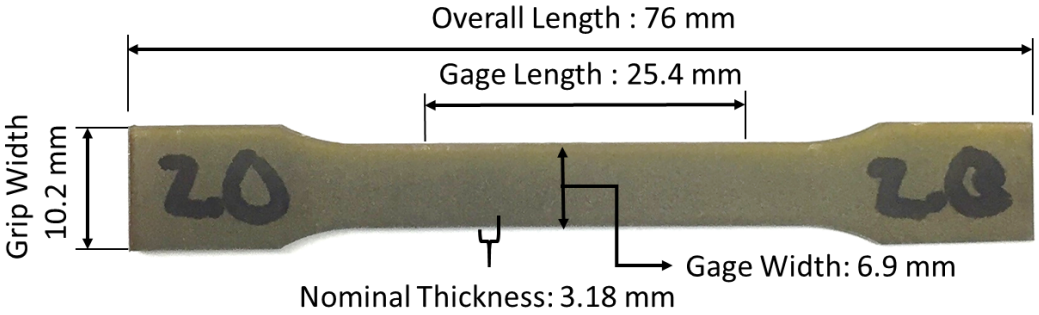

Figure 4.7: Geometry of machined tension specimen.

Testing specimens were created by machining a section of the damaged pressure vessel into two sets parallel tensile specimens that span the thickness of the pressure vessel wall. The shape of these specimens is shown Figure 4.7. Tensile specimens were machined using electrical discharge wire cutting to remove material until the desired shape was created. Next, nine horizontal cuts were made along the thickness of the pressure vessel to create two sets of eight tensile specimens shown in Figure 4.8. Each set was treated individually while testing.

As can be seen, the two sets of specimens have been cut from the original test piece spanning the thickness, note that specimens 1.1 through 1.8 and 2.1 through 2.8 have increasing depths from the outside surface, meaning 1.1 and 2.1 are closest to the outside surface and 1.8 and 2.8 are closest to the inside surface. The depth of each specimen is defined by the distance of the centroid to the outside surface of the pressure vessel. Each specimen has a graded damage level throughout its thickness because the level of damage increases with depth from the outside surface. Because of the graded damage level, the material response should be considered an average response across the thickness of the specimen rather than just the response at the depth defined by the centroid.

The testing procedure for tensile testing was completed as follows: Each specimen was measured with digital calipers to determine the thickness and width of the gage. These measurements were used to determine the effective area. After the dimensions were measured, tensile specimens were placed in the Instron model 4400 load frame, ensuring the grips on each end were centered and secured by the machine clamps. Each specimen was aligned vertically with roughly 1 mm of the grip was exposed. Next, the extensometer was fixed to the center of the gage section of the specimen. For reference, see Figure 4.9, which displays the testing configuration and loaded specimen. Each test had the displacement set to a constant value of 2 mm/second. Load and position data were collected for each specimen with a frequency of 2 Hz. Strength values were estimated based on specimen dimensions and the recorded load. Strain data was determined by percent elongation of the specimen as measured by the extensometer, which has a nominal gage length of 25.4 mm.

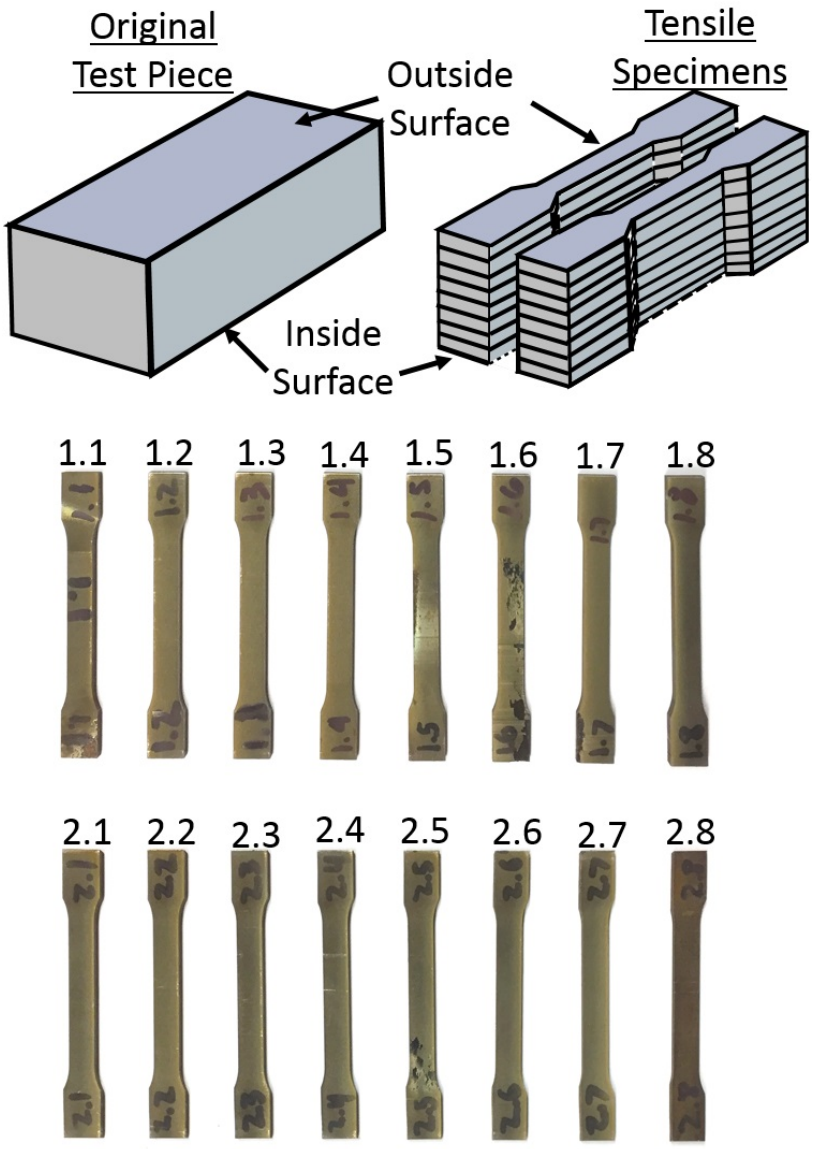

Figure 4.8: Illustration of tensile specimen locations within the test piece.

Figure 4.9: Tensile specimen loaded in the Instron model 4400 load frame with the extensometer attached and centered.

4.4 Microscopy

In conjunction with the testing described previously, scanning electron microscopic images were also taken of a separate specimen. This specimen originates from the same pressure vessel as the previous testing specimens. Due to the original size of the specimen, it was first cut into small rectangular sections with the rough dimensions 30 mm by 17 mm by 16 mm. Then, to ensure clear pictures from the microscope, the surface of the specimen was successively polished down to a scale of 0.25 microns. Polishing allows the HTHA damage features to be distinct on the surface of the test piece. The microscope used was the JEOL 7000F analytical scanning electron microscope. This microscope allows for magnifications from 10x up to 500,000x. Additionally, the microscope can be used to determine composition of scanned areas. A picture of the imaging microscope can be found in Figure 4.10. Specimens were scanned near the inside surface to identify damaged areas.

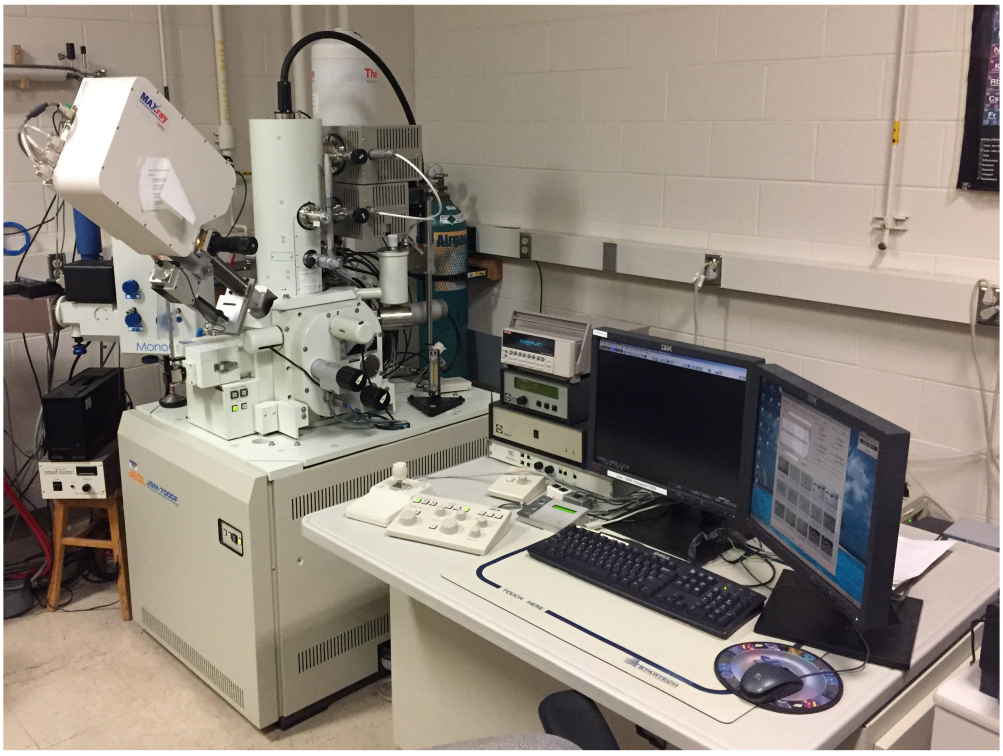

Figure 4.10: Microscopic imaging configuration. The JEOL 7000F analytical Scanning electron microscope is pictured.

CHAPTER 5

RESULTS

5.1 Non-Collinear Wave Mixing Results

Nonlinear waves were received as a result of the non-collinear wave-mixing of two primary shear waves. Figure 5.1 is an example of the time domain response of the primary waves, inverted primary waves, sum of the inverted and non-inverted primary waves, and the filtered sum displaying the nonlinear signal. The time-of-arrival matches closely ($\pm 5\%$) with the predicted time obtained from straight ray path analysis. In the case shown in Figure 5.1, the expected arrival time was 0.0238 milliseconds, and the nonlinear scattered wave arrived at 0.0244 milliseconds. Time of arrival criteria was checked for each trial at each depth to ensure the observed signal was originating from nonlinear interaction. Figure 5.2 contains the nonlinear wave generation parameter corresponding to the distance from the outside surface. These parameters were normalized with the nonlinear wave generation parameter which corresponds to the material layer closest to the outside surface as described in Section 3.3. This is the point corresponding to 0.1 cm depth or Point A in Figure 5.2. The error bars included on the graph in Figure 5.2 correspond to the maximum and minimum trial values at that particular depth. Because all measurements were conducted independently, there was variability between tests which illustrates the damage variability in the specimen at a particular depth. Different values were obtained by spacing the primary wave wedges at varying distances on the inside and outside surface of the specimen, allowing measurements throughout the thickness (0.1 cm - 2.9 cm) of the specimen.

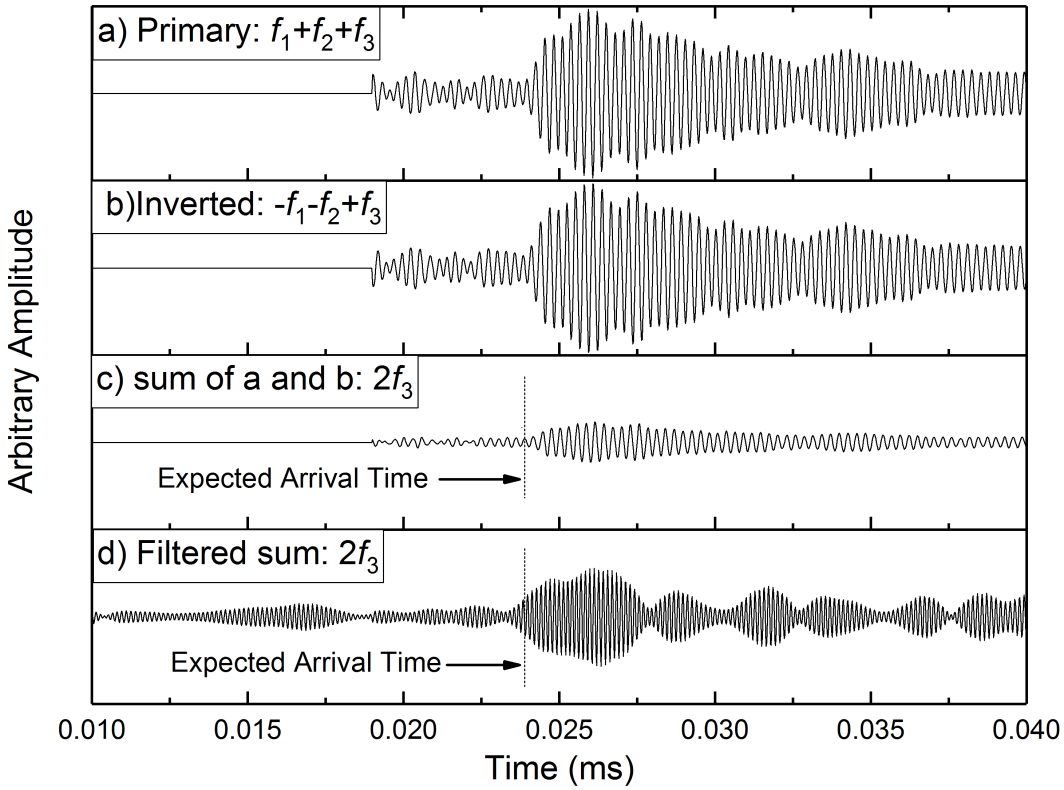

Figure 5.1: Plot a shows the time domain record of simultaneous operation of both primary transducers, plot b shows the time domain record of the inverted simultaneous operation of both transducers, Plot c shows the summation of Plots a and b, and Plot d shows the filtered plot of the summation. Note that the expected arrival time is shown.

As can be seen in Figure 5.2, the trend in the normalized wave generation parameter illustrates the damaged caused by HTHA within the pressure vessel wall. It is worth pointing out that significant damage does not appear to begin until roughly two centimeters through the thickness of the pressure vessel. The concentrated accumulation of damage is near the inside surface, which coincides with the progression of HTHA. At shallower depths, near the outside surface, all tests had relatively low normalized β parameters around or below 1. Note that fluctuations of the normalized β parameter around or below 1 indicate that there is no change in the amount of damage at that particular depth.

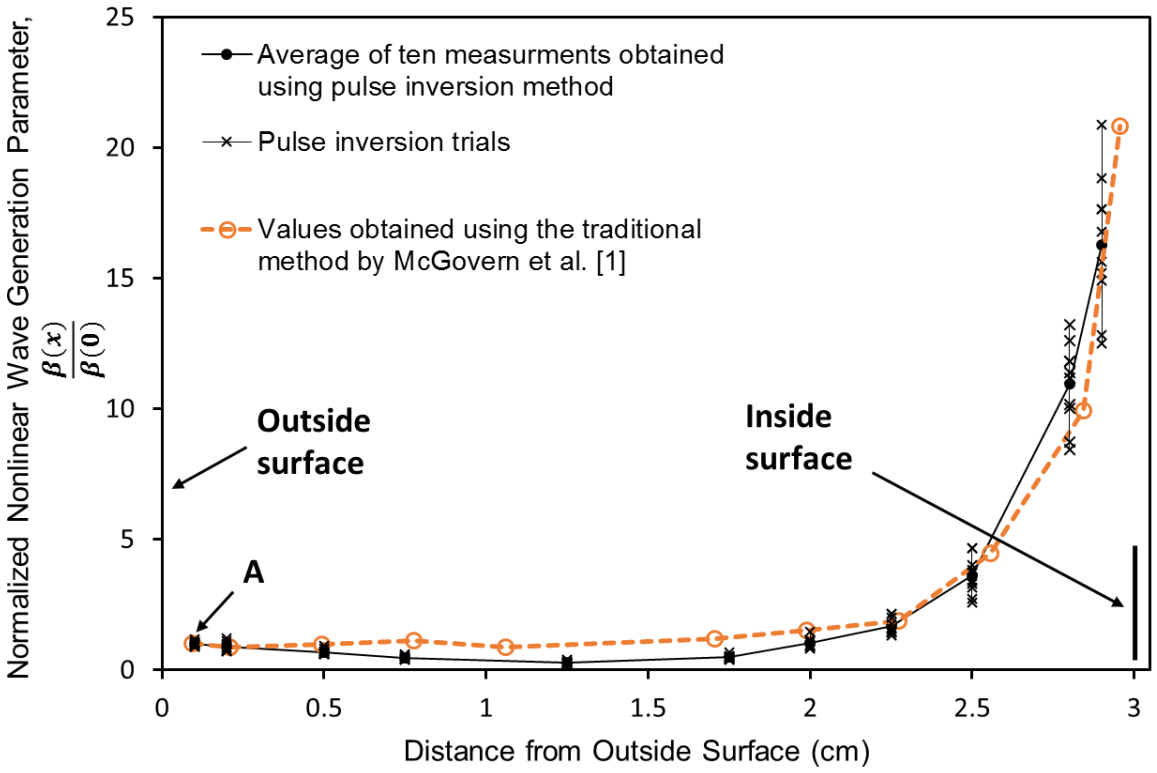

Figure 5.2: Normalized nonlinear wave generation parameter versus the distance from the outside surface. Note that the error bars overlap since distances between measurement depths are smaller than the characteristic length of the interaction region. The shape of the normalized nonlinear wave generation parameter versus distance illustrates the pattern of HTHA damage through the thickness of the pressure vessel wall.

For the configuration that was used in this study, the beam divergence of the primary waves is very small. In this particular case, it is significantly lower than 1°, 1.5×10^{-6} °. Therefore, beam spread should not significantly change the volume of interaction for each measurement depth. Therefore, at each measurement depth, the characteristic length of the volume of interaction is 1.25 cm, or the effective diameter of the primary wave transducers. In part, variability in the measurements of the normalized nonlinear wave generation parameter can be attributed to the relatively large volume of interaction compared to the distance between measurement depths throughout the thickness. Measurement depths have distances between them smaller than the characteristic length of the volume of interaction. This can cause overlap between different measurement depths.

Additionally, since transducers were removed and replaced prior to each trial, the volume of interaction varies during the testing trials. Due to greater variability in damage near the inside surface, replacing the transducers results in different interaction locations at the same depth, further increasing variability. These factors account for overlapping error bars at different measurement depths, as can be seen in Figure 5.2.

In addition to the data points gathered from the pulse inversion technique, Figure 5.2 also contains data values that were obtained with permission from McGovern et al. [1]. McGovern used the subtraction method for nonlinear interrogation. This method of analysis for the nonlinear wave generation parameter is similar to the pulse inversion method, but relies on the addition of the individual signals from primary wave transducers, and then subtracting this sum from the signal received from simultaneous operation. Notice that the curves in Figure 5.2 correspond well throughout the thickness. This demonstrates the reliability of the nonlinear interrogation methods used for this characterization. It is worth noting the pulse inversion method results in a nonlinear wave amplitude twice as large as what would be seen in the subtraction method used by McGovern. This allows for clearer identification of the nonlinear signals and can reduce the uncertainty during tests.

5.2 Tensile Strength Results

Tensile strength testing was completed on tensile specimens machined from the same retired pressure vessel that was probed using non-collinear wave mixing. Specimens were machined at various distances throughout the thickness of the pressure vessel (see Figure 4.8) which allowed for comparison between non-collinear wave mixing results and tensile results. Stress-strain data was collected for each of the specimens. A summary of values obtained from the tensile specimens can be found in Table 5.1. Please note that specimens 1.5, 1.6, 2.4, 2.5, and 2.6 were severely damaged, causing the specimens to fail along cracks. Because these specimens failed along cracks, the effective area is reduced compared to the measured cross section. This causes in difficulty in estimating the strength so these specimens were omitted from the tensile results.

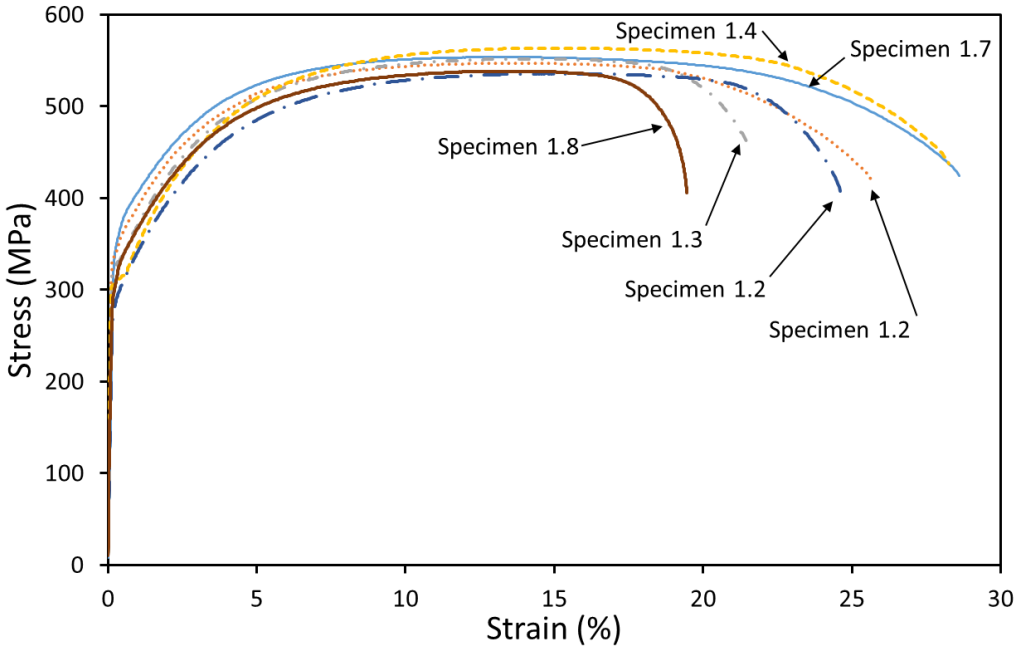

Figure 5.3: Stress Strain relationships for all tensile tests from specimen set one, excluding 1.5 and 1.6 due to severe damage.

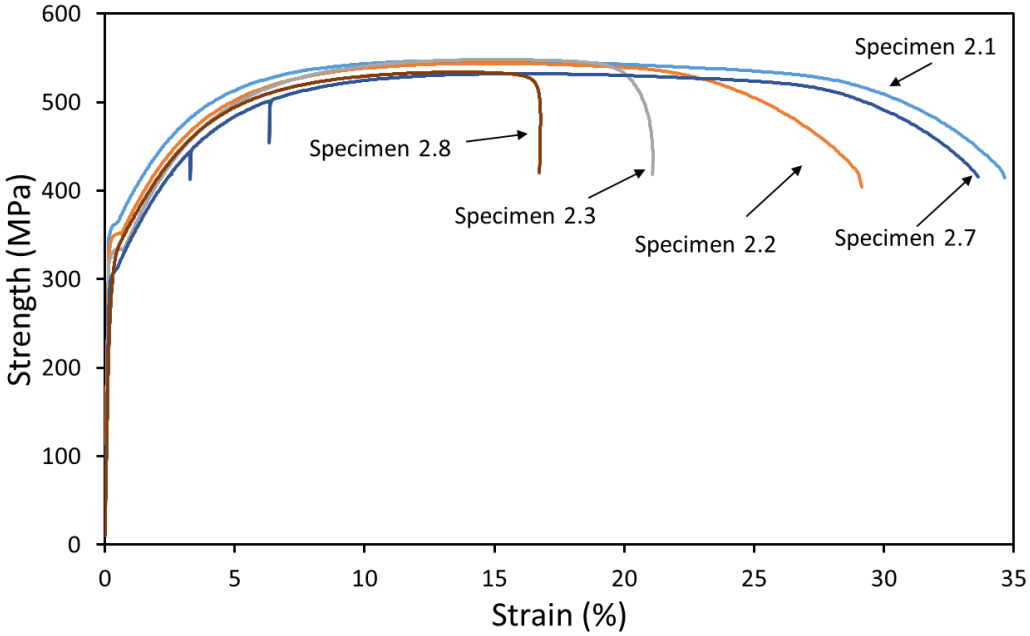

Figure 5.4: Stress Strain relationships for all tensile tests from specimen set two, excluding 2.4, 2.5 and 2.6 due to severe damage.

All of stress strain curves are displayed in Figures 5.3 and 5.4. Notice that there is a significant variability in the data throughout the specimen. This is an indication of the localized and stochastic nature of HTHA damage throughout the thickness of the pressure

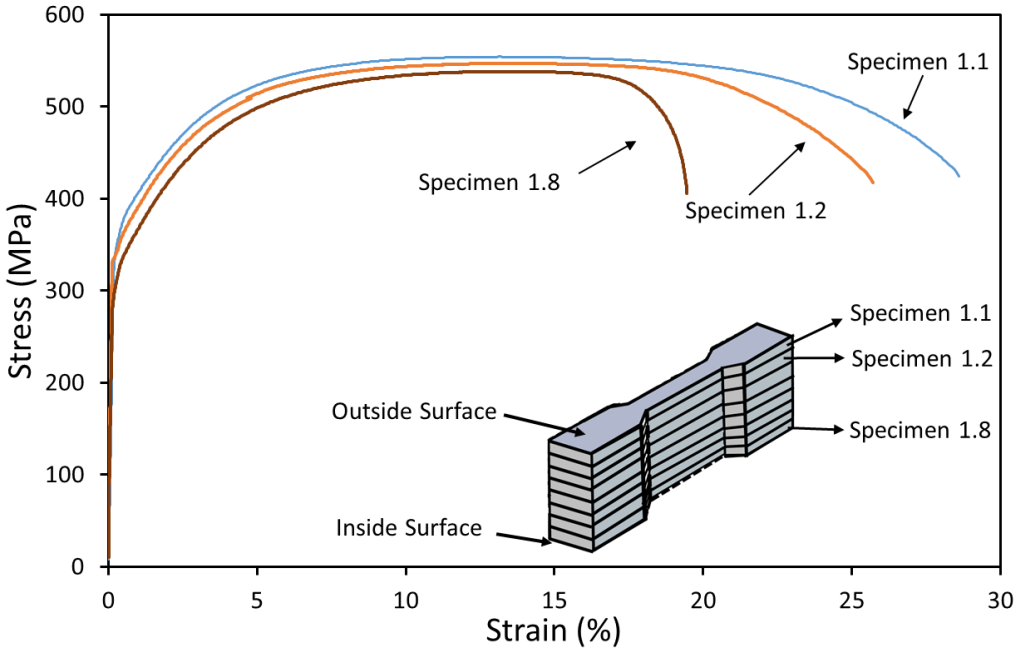

Figure 5.5: This figure illustrates the stress-strain relationship for specimens 1.1, 1.2, and 1.8. Note the distinct difference between the strength values of each specimen.

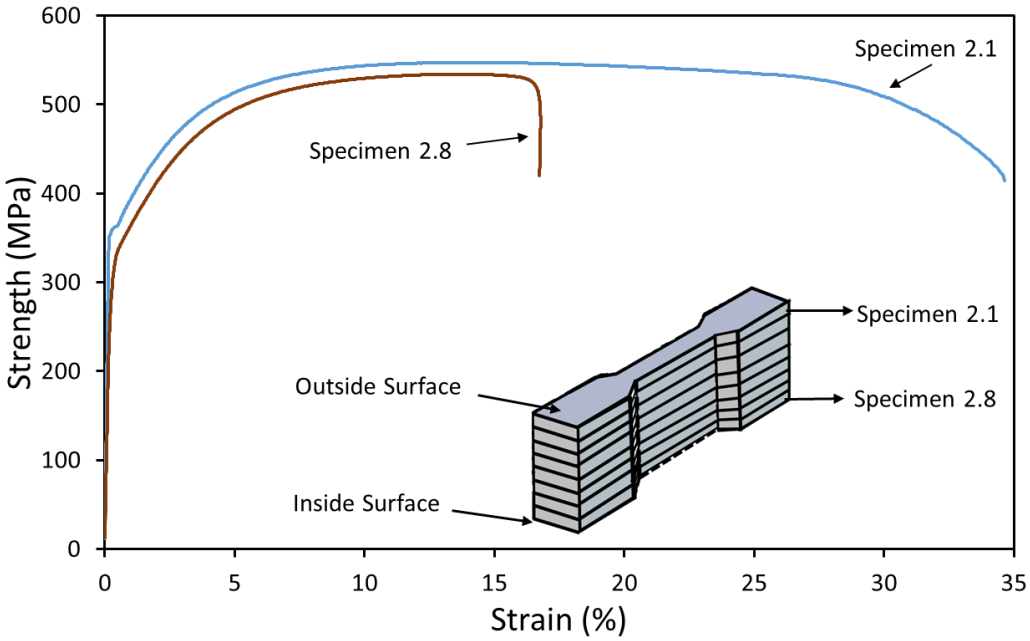

Figure 5.6: Figure illustrates the stress-strain relationship for specimens 2.1 and 2.8. Note the distinct difference between the strength values of each specimen.

vessel. A clearer example of the tensile data is shown in Figures 5.5 and 5.6. These figures display the distinct differences in material response from specimens near the inside surface and outside surface. Note that there is a clear drop in strength for specimens 1.1 and 1.8 in

Table 5.1: Results from tensile tests

Specimen Set Number One								
Specimen	Depth (mm)	Thickness (mm)	Width (mm)	Area (mm^2)	Max Load (kN)	UTS (Mpa)	Yield strength (Mpa)	Failure Strain (%)
1.1	1.82	3.19	6.90	22.00	12.17	553.22	314.25	28.73
1.2	5.20	3.17	6.90	21.90	11.98	547.13	321.84	25.70
1.3	8.58	3.18	6.91	22.00	12.14	551.90	320.86	21.96
1.4	11.96	3.17	6.91	21.94	12.36	563.40	304.22	28.26
1.5*	15.34	3.19	6.92	22.04	9.55	433.24	242.96	2.12
1.6*	18.71	3.17	6.91	21.88	6.42	293.53	N/A	0.94
1.7	22.09	3.18	6.92	22.01	11.78	535.32	268.20	24.62
1.8	25.98	4.21	6.92	29.10	15.66	538.22	265.08	19.46
Specimen Set Number Two								
Specimen	Depth (mm)	Thickness (mm)	Width (mm)	Area (mm^2)	Max Load (kN)	UTS (Mpa)	Yield strength (Mpa)	Failure Strain (%)
2.1	3.89	3.19	6.91	22.03	12.05	546.93	337.00	34.66
2.2	7.23	3.19	6.91	22.03	11.98	543.79	328.95	29.16
2.3	10.57	3.20	6.92	22.14	12.14	548.23	322.34	21.09
2.4*	13.89	3.15	6.91	21.77	8.70	399.47	256.17	12.83
2.5*	17.20	3.16	6.93	21.91	9.88	451.09	260.41	3.53
2.6*	20.52	3.18	6.93	22.01	11.29	512.85	215.95	15.42
2.7	23.85	3.18	6.92	22.03	11.73	532.49	285.00	33.62
2.8	26.92	2.67	6.91	18.43	9.84	534.06	252.00	16.74

* Due to severe damage within the original test piece, these tensile specimens failed along large cracks within their cross section. This causes difficulty in estimating the stress within the specimen. Consequently, these specimens were excluded from further analysis and not included in Figures 5.3 and 5.4.

Figure 5.5 and for specimens 2.1 and 2.8 in Figure 5.6. Tension data was further analyzed to obtain ultimate strength and yield strength. Ultimate strength was obtained simply by finding the maximum stress during the tension test. Yield strength was estimated for each specimen by finding the point where the material response deviated from linear elastic behavior. This was accomplished by determining the slope of the linear elastic region and plotting a parallel line over the original stress strain curve. Then a point was identified on the stress-strain curve where the curve deviates from the overlapping line. This process is illustrated in Figure 5.7.

Figure 5.8 shows the percent reduction in strength versus the distance through the specimen. Each yield strength value was normalized relative to a bilinear trend indicating the average yield strength of specimens close to the outside surface. Using these normalized values, a percent reduction in yield strength was estimated and plotted in

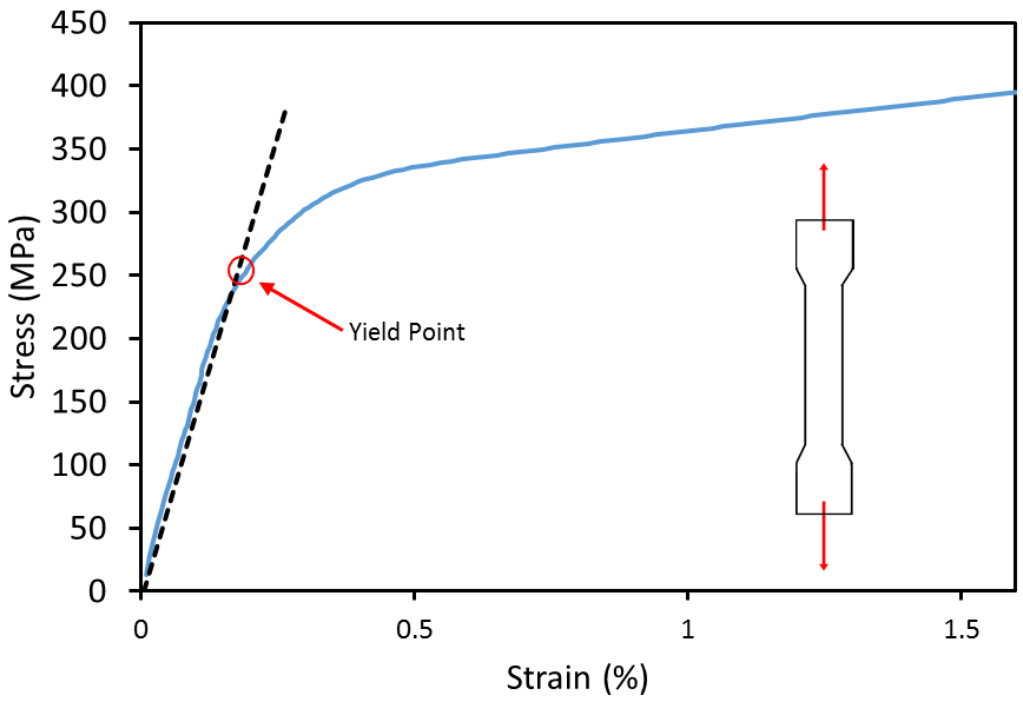

Figure 5.7: Estimation of yield strength by identifying the point where the stress-strain curve deviates from linearity.

Figure 5.8. This figure illustrates that the reduction in strength increases as the depth increases. This is can be seen for both specimen sets. Specimens near the outside surface have a distribution around 0% reduction, while specimens 1.7, 1.8, 2.7, and 2.8 all have a large reduction in yield strength. The loss in strength is due to microvoids and small fissuring that is present in the specimens closer to the inside surface and loss of carbon caused by the formation of methane. Microvoids and fissuring reduce the effective area of the tensile specimens contributing to the loss in strength. And as carbides are pulled out of the metal micro-structure, the strength properties of the metal are negatively affected [45]. This is consistent with the nonlinear results which do not show drastic change in the nonlinear parameter until the interaction depth approaches 1 cm from the inside surface.

Similarly, the ultimate strength values obtained from the tensile specimens closer to the inside surface are less than those than the ones near the outsider surface. This is illustrated in Figure 5.9. Each of these figures illustrates the reduction of strength in the specimens closer to the inside surface. In addition, these figures show that the nonlinear

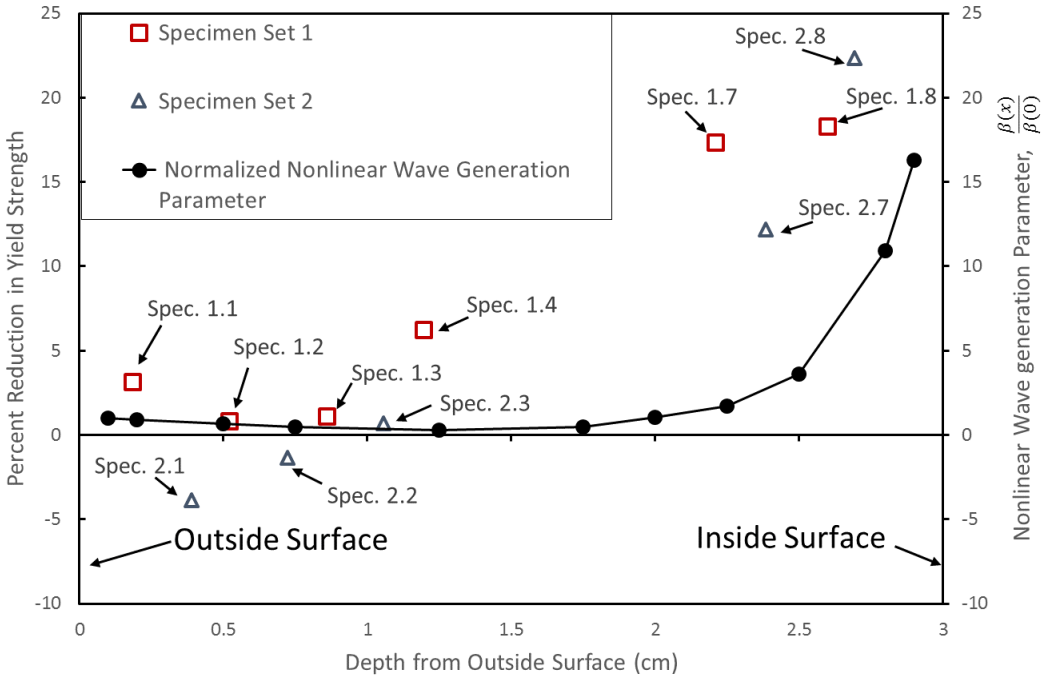

Figure 5.8: Normalized nonlinear wave generation parameter and percent reduction in yield strength versus distance from the outside surface. This figure illustrates the relative reduction in yield strength with an increase of the nonlinear wave generation parameter.

results are a good indicator of the significant damage increase towards the inside surface of the pressure vessel.

In addition to loss in strength, HTHA damage is known to decrease ductility through decarburization. Studies have shown that loss in ductility via the reduction in tensile elongation is a consequence of HTHA damage [18]. To illustrate this, strain measurements were recorded during this study. However, there was some difficulty in measuring ductility due to the small size of the specimens relative to the extensometer. Failure regions sometimes occurred outside the span of the extensometer, this can cause some of elongation values to be smaller than the true values since the extensometer does not record elongation outside of its span. Despite the difficulties, the decreasing percent elongation trend is supported from the data obtained during this study observing the outermost and innermost specimens for each set. Specimen 1.1 and 2.1 have failure strains of 29 % and 35 % respectively, while 1.8 and 2.8 had failure strains of 19 % and 17 %. Specimen set 1 and specimen set 2 have a decrease in percent elongation of 10 % and 16 %, respectively. This

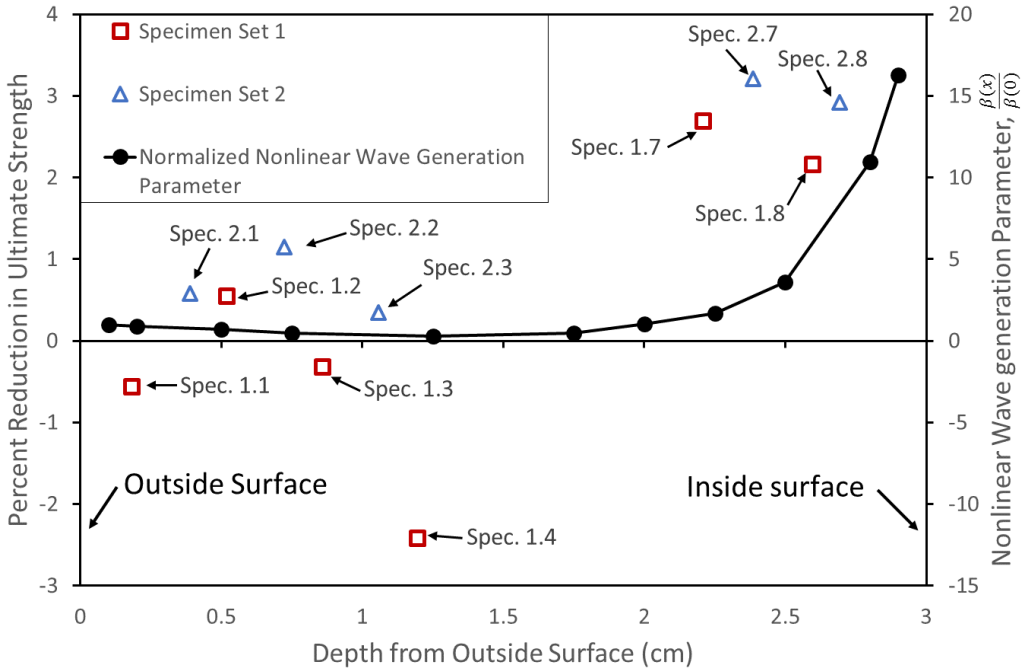

Figure 5.9: Normalized nonlinear wave generation parameter and percent reduction in ultimate strength versus distance from the outside surface. This Figure illustrates the relative reduction in ultimate strength with an increase of the nonlinear wave generation parameter.

implies that a decreasing trend in ductility is present through the pressure vessel wall.

These results have shown that the strength and ductility properties of the pressure vessel were negatively affected by HTHA damage. There is still need for more work to be done. The data set provided for this study was limited to 16 total specimens, and 5 of these specimens were severely damaged and provided little useful information. From the data that was available, there was a clear difference between the specimens at the outside surface and the specimens at the inside surface. Namely, specimens machined from sections near the inside surface are weaker and less ductile. Unfortunately many of the specimens at depths near the center of the pressure vessel wall failed, and there is currently an incomplete representation of this trend. In the future, more work needs to be done on additional specimens machined from similar vessels. One important step that can be made in the future is to probe the specimen with pulse echo measurements to ensure there are no large cracks spanning the area from which the specimens will be machined. This will prevent specimens from having severe cracks that will impede the data collection process.

5.3 Microscopy

Additional analysis was conducted by taking microscopic images of a section of the damaged steel pressure vessel with an scanning electron microscope. Microscopy is a method that has been widely used in the identification of HTHA damage, microscopy also provides a means to understand the initiation, growth and composition of HTHA damage [4, 18, 45, 46]. It has been noted that microscopy on a scale of roughly 5 microns can identify very small (1μm) microvoids initiating along grain boundaries. In more advanced stages, and rather suddenly, coalescence of microvoids results in blistering and fissuring which can lead to detrimental cracking. For the sample specimens received for this study, advanced HTHA damage has occurred. Examples of the voids and fissuring can be found in the figures below, each successive image has increased magnification. Note that the images shown display the scale in the lower right hand corner.

Figure 5.10 displays the various levels of severity that can result from HTHA, including large macroscopic cracking, small microvoids, and small microcracks. Increasing the magnification allows more damage to be identified, Figure 5.11 shows the density of the microvoids and cracks that have formed near the inside surface of the specimen. Figure 5.11 clearly shows the severity of HTHA in this particular sample. The damage is shown in even more detail in Figure 5.12 where small fissures where microvoids have coalesced have formed cracks and additional voids are visible. Figure 5.13 highlights the detail of one of these microcracks. In the same area this image was taken, a compositional analysis was completed along the crack. The results showed that the crack is composed of magnesium sulfide. This is common among the microcracks visible using the scanning electron microscope. The reason for these cracks forming along pockets of magnesium sulfide is because areas where these planar inclusions are present are more susceptible to HTHA damage [18]. Magnesium sulfide inclusions are highly susceptible to HTHA damage because they become flat or "pancaked" planar inclusions during the rolling process when the steel is formed. The images shown within this section illustrate that HTHA damage is extremely advanced in these specimens which further verifies the results from the previous tests.

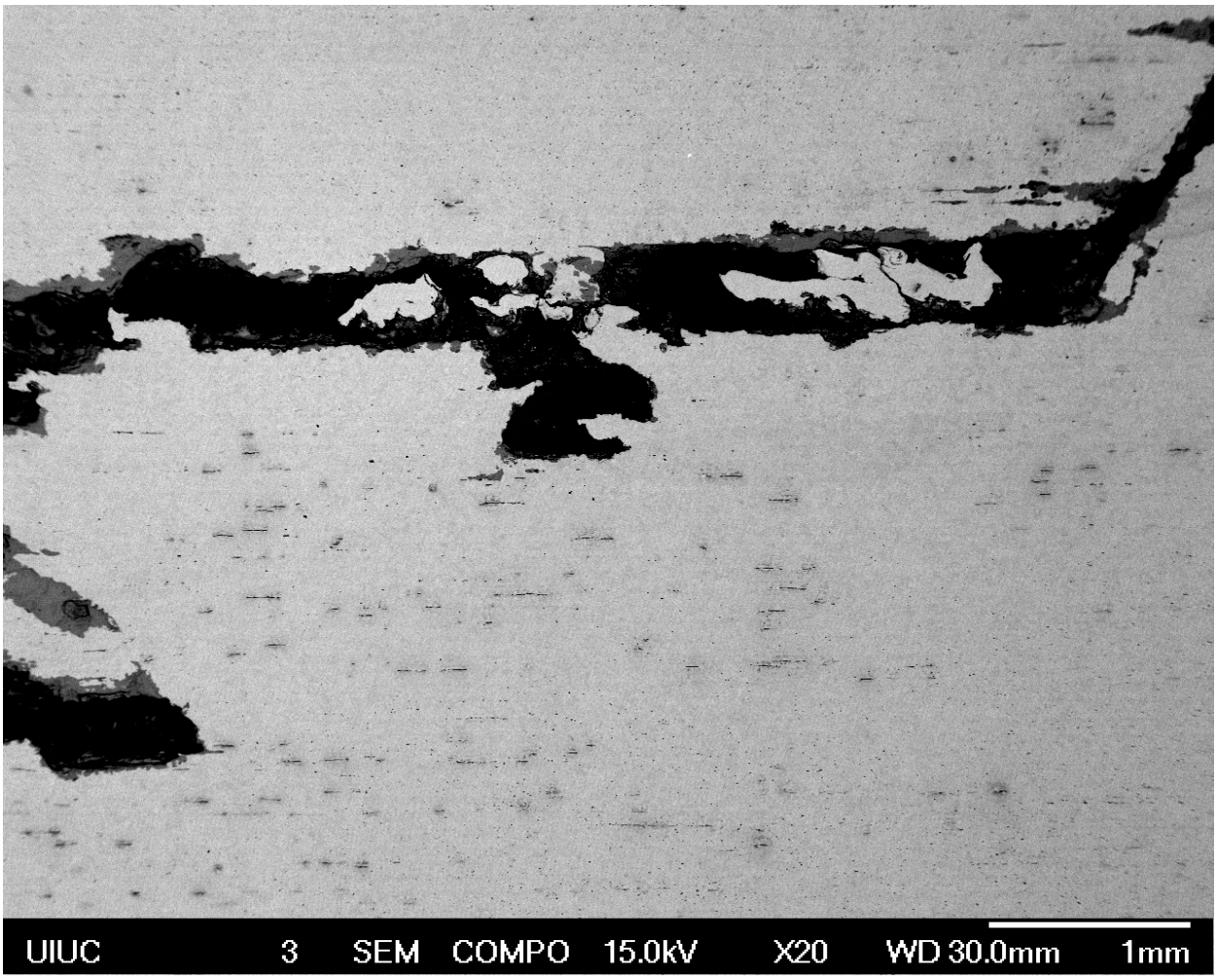

Figure 5.10: This image displays 20x magnification a large macroscopic crack which runs through the specimen, additionally numerous small cracks and voids can be seen below the larger crack. The location of this image is roughly 1 cm from the inside surface.

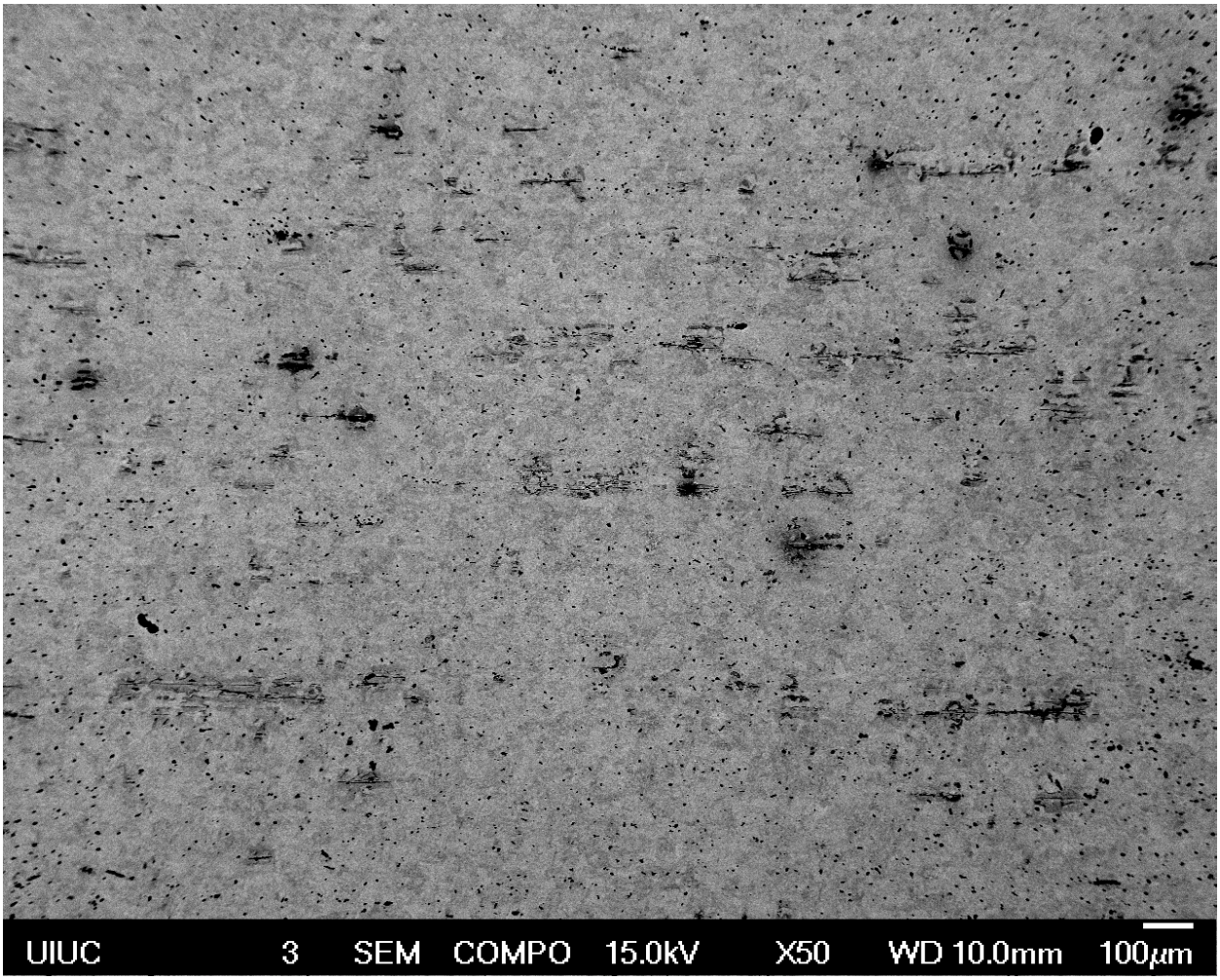

Figure 5.11: This image displays a 50x magnification of the region below the large crack (closer to the inside surface) filled with numerous voids and small fissures.

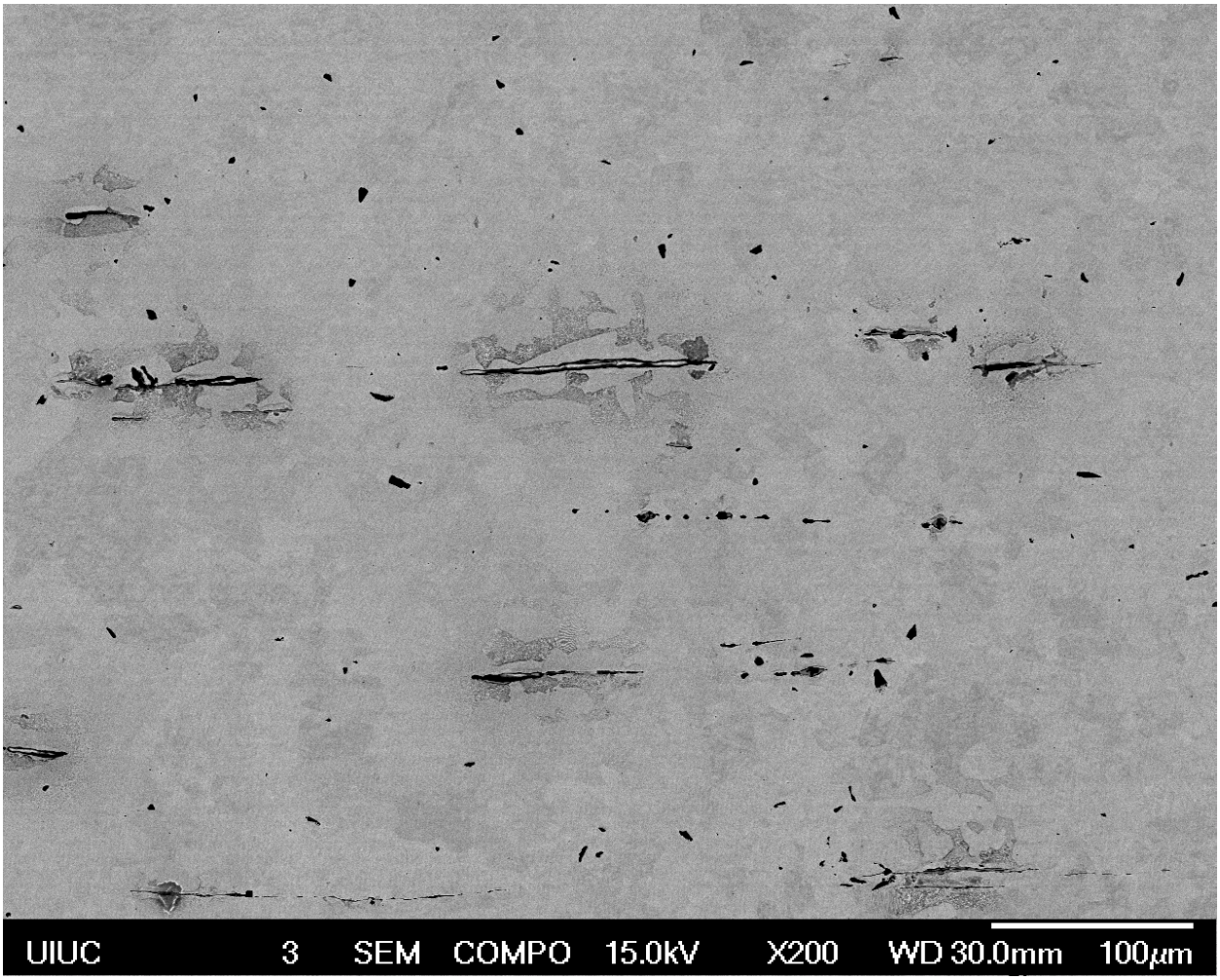

Figure 5.12: This image displays a 200x magnification of the region below the large crack (closer to the inside surface).

Figure 5.13: This image displays a 750x magnification of a particular microcrack found in 5.12. Note that the dark regions around the microcrack display a pearlitic microsctructure composition.

CHAPTER 6

CONCLUSION

A highly damaged HTHA specimen was probed using non-collinear wave mixing; tested in tension for various degrees of damage; and microscopic images were recorded near the inside diameter of the specimen. Each of these techniques confirmed the presence of HTHA damage in the steel specimen.

Non-collinear ultrasonic wave mixing measurements were performed using a pulse inversion method on a retired steel pressure vessel subject to significant HTHA damage. The Normalized nonlinear wave generation parameter, $\beta(x)/\beta(0)$, was used to characterize the degree of damage within the sample. Nonlinear behavior was measured throughout the thickness of the sample. The nonlinear behavior stayed relatively constant until roughly 2 cm from the inside surface, where the highest degree of nonlinearity is found. At the depth closest to the inside surface, the nonlinear wave generation parameter increased by a factor of 16 relative to the normalization point, indicating a large increase in HTHA damage.

The pulse inversion technique was also compared to a non-collinear study conducted previously by McGovern [1]. The nonlinear results from the study by McGovern correspond well with the pulse inversion trials conducted in this study. The consistency of these results illustrate the reliability of the testing method for detection of HTHA. Additionally, by using the pulse inversion technique, the signal to noise ratio for nonlinear signals is significantly increased due to constructive interference in the nonlinear wave caused by the summation primary and inverted primary time domain records. This provides a clearer and more easily identifiable nonlinear signal.

The non-collinear method was shown to be possible with access only to the outside surface of the specimen. This was accomplished by using pulse echo, subsurface longitudinal wave, and Rayleigh wave measurements to estimate attenuation values within the specimen. An important result of this study is illustrating single sided measurements of HTHA damage are possible. These results make the non-collinear wave mixing technique particularly attractive for in-situ inspection.

Coinciding with the non-collinear wave mixing measurements, tensile strength tests were conducted on tensile specimens. Two sets of tensile specimens were created at various depths through the thickness of the same pressure vessel probed using non-collinear wave mixing. This allowed for comparisons to be drawn from results of the two tests. Tensile strength testing showed that the two sets of tensile specimens had a decrease in yield strength of 18% and 23% for sets 1 and 2, respectively. A decrease in ultimate strength of up to 3 % for sets 1 and 2. And a decrease in percent elongation of 10% and 16%, for sets 1 and 2, respectively. Both sets saw a significant decrease in strength and ductility as the depth from the outside surface increased. These tensile results further validated the non-collinear wave mixing results, showing that an increased level of damage measured from nonlinear interrogation coincided with reduced yield strength, reduced ultimate tensile strength, and reduced percent elongation.

Lastly, scanning electron microscope images were taken on a cross section of the steel pressure vessel displaying advanced stages of damage, further validating the results from non-collinear wave mixing and tensile tests. Tensile testing and microscopic imaging confirm the viability of non-collinear wave mixing as a detection and characterization method for nondestructive evaluation of high temperature hydrogen attack.

CHAPTER 7

FUTURE RECOMMENDATIONS

7.1 Single Sided In-situ Inspection

A common theme throughout this study involved using the non-collinear wave mixing technique as a single sided approach for HTHA damage inspection. The results above show the viability in using this process. However, the tests performed in this study were performed at room temperature in a laboratory setting. The next step for this work is to duplicate non-collinear measurements on a pressure vessel under working conditions. Under these conditions, the steel will be under stress caused by the internal pressures, the steel will be at operating temperatures, and the methane bubbles trapped within the microstructure will be at high pressures. All of these factors can change the results and procedure for non-collinear wave mixing. It would also be beneficial to conduct tensile testing on specimens near working temperatures. This would give a better indication of the stress levels near the inside surface of a pressure vessel which can initiate catastrophic failures.

A few important factors which should be discussed about in-Situ inspection are the change in the levels of stress present, the change in the methane bubble pressure, and the change in operating temperature. First, the levels of stress present in the pressure vessel can change the velocities of the primary waves, and scattered wave. This is a phenomenon called the acoustoelastic effect. The acoustoelastic effect is the change in the speed of elastic wave propagation in a body that is simultaneously undergoing static elastic deformation [6, 47]. Using non-collinear wave mixing on an in-situ pressure vessel may cause the incident angles for the primary wave transducer wedges and predicted arrival

times for the nonlinear scattered waves to change because of this affect. Therefore, it is necessary to understand how the change in velocity for various pressure levels will affect these measurements. Next, the change in the methane bubble pressure must be considered. Because the tests run in this study were ate room temperature, it is possible that the pressures of the trapped methane were significantly reduced. This can have an effect on the overall nonlinearity of the microstructure, and therefore the amplitude of the scattered waves. During operating conditions, the nonlinearity in the pressure vessel will be affected by the presence of trapped methane at higher pressures. This must be taken into consideration while taking measurements at the operating conditions. Lastly, higher temperatures present at operating conditions need to be accounted for. High temperatures can affect the material response as compared to room temperature inspection, this may have an effect on the nonlinear response and possibly the mechanical response as well. Additionally, it is important to ensure that testing equipment will not be damaged from exposure to high temperatures. The issues highlighted above need to be considered before taking the next step towards in-situ inspection.

7.2 Collinear Wave Mixing for Nonlinear Interrogation of Steel

The results shown above have proven the great potential to using nonlinear wave mixing to inspect materials. Not only does it allow for better resolution of micro structural damage in many cases, but is also offers new strategies for in-situ inspection. Some of the most attractive potential wave mixing techniques are through use of collinear cases. Collinear wave interaction is similar to non-collinear wave mixing, but the angle of interaction φ is 0° for a for a collinear interaction, or 180° for a collision interaction, in other words the condition from equation 3.4 is equal to 1 or -1 respectively. For this section, one possible alternative case will be discussed in relation to two potential configurations for the single-sided ultrasonic inspection. This particular case is a pulse-echo method of detection using collinear wave mixing, the section below will discuss some of the possible options for experimental use of this methods. Note that the collinear cases described in this section do meet the polarization and resonance conditions required for the production of a scattered

wave [38].

The first case that will be discussed is the pulse-echo method of collinear wave mixing. In this particular case, the primary waves are a shear wave and longitudinal wave. The longitudinal wave catches up to the shear wave to create a scattered longitudinal wave of a difference frequency. This particular case is interesting because this method can be done on a single side of a specimen and has the potential to be programmable meaning that the interaction region can be simply predetermined without moving the testing configuration. Consider Figure 7.1, this illustrates the simple testing set up that would be possible using this collinear case. As can be seen from the diagram, this involves a difference frequency longitudinal scattered wave, and also requires that the scattered wave come directly backwards to strike the pickup transducer, this puts constraints on this testing set up

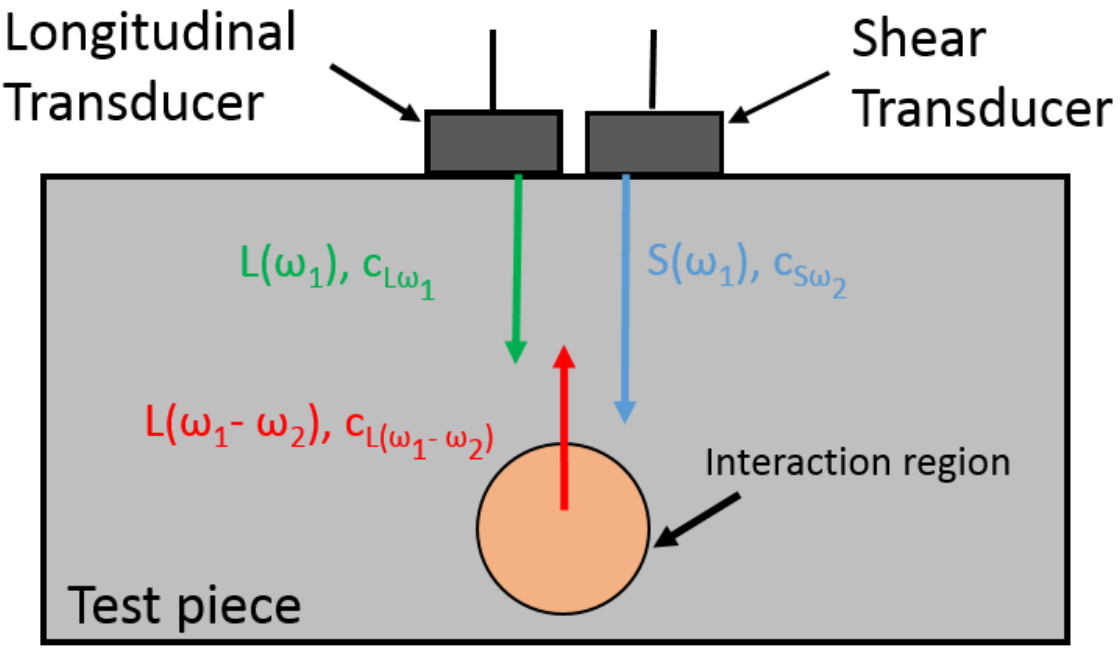

Figure 7.1: Schematic representation of a potential alternative configuration for single sided nonlinear interrogation of HTHA.

based on the resonance conditions for this case.

Many parameters need to be known prior to conducting this test these include the velocities and attenuations for all traveling waves at the respective frequencies, i.e., shear velocity at a frequency of ω_2, longitudinal velocity at both frequencies of ω_1 and $\omega_1 - \omega_2$ and corresponding attenuations. Note that, depending on the material velocities can change with frequency [41]. With knowledge of the primary wave velocities, the interaction region can be predetermined based on the time of arrival of the primary waves to the desired region of interaction. This requires a time delay between the triggering of the primary shear wave and the longitudinal wave transducers. The delay would simply need to be the difference in the time of flights of the primary waves it can be expressed as Equation 7.1

$$t_{delay} = d\left(\frac{1}{c_S} - \frac{1}{c_L}\right) \tag{7.1}$$

Where d is the desired interaction depth of the primary waves, c_S and c_L are the primary shear wave speed and the longitudinal wave speed respectively. Varying the time delay can allow for multiple depths throughout the specimens to be measured simply through adjusting the time delay function.

In addition to having a computerized delay function it is also possible to utilize a wave guide for nonlinear interaction. The longitudinal transducer could be placed on a wave guide with specific thickness to ensure an interaction in the correct region. However, this can prove difficult since various wave guides of different thicknesses would be needed to scan multiple depths. A possible solution to this would be to utilize a wave guide in conjunction with angle-beam wedges. Longitudinal and shear waves can be induced from longitudinal transducers at critically refracted angles, such that the primary shear and longitudinal waves travel parallel to the surface of the wave guide. By staggering the angled wedges on the wave guide, it is possible to delay the longitudinal wave for long enough to ensure interaction in the correct region. Please see figure 7.2. Using this configuration, it is not necessary to program a system delay. In this case, the location of the angled wedges can be adjusted to move the volume of interaction to a new location. However this configuration has many disadvantages as well. Due to the angled wedges

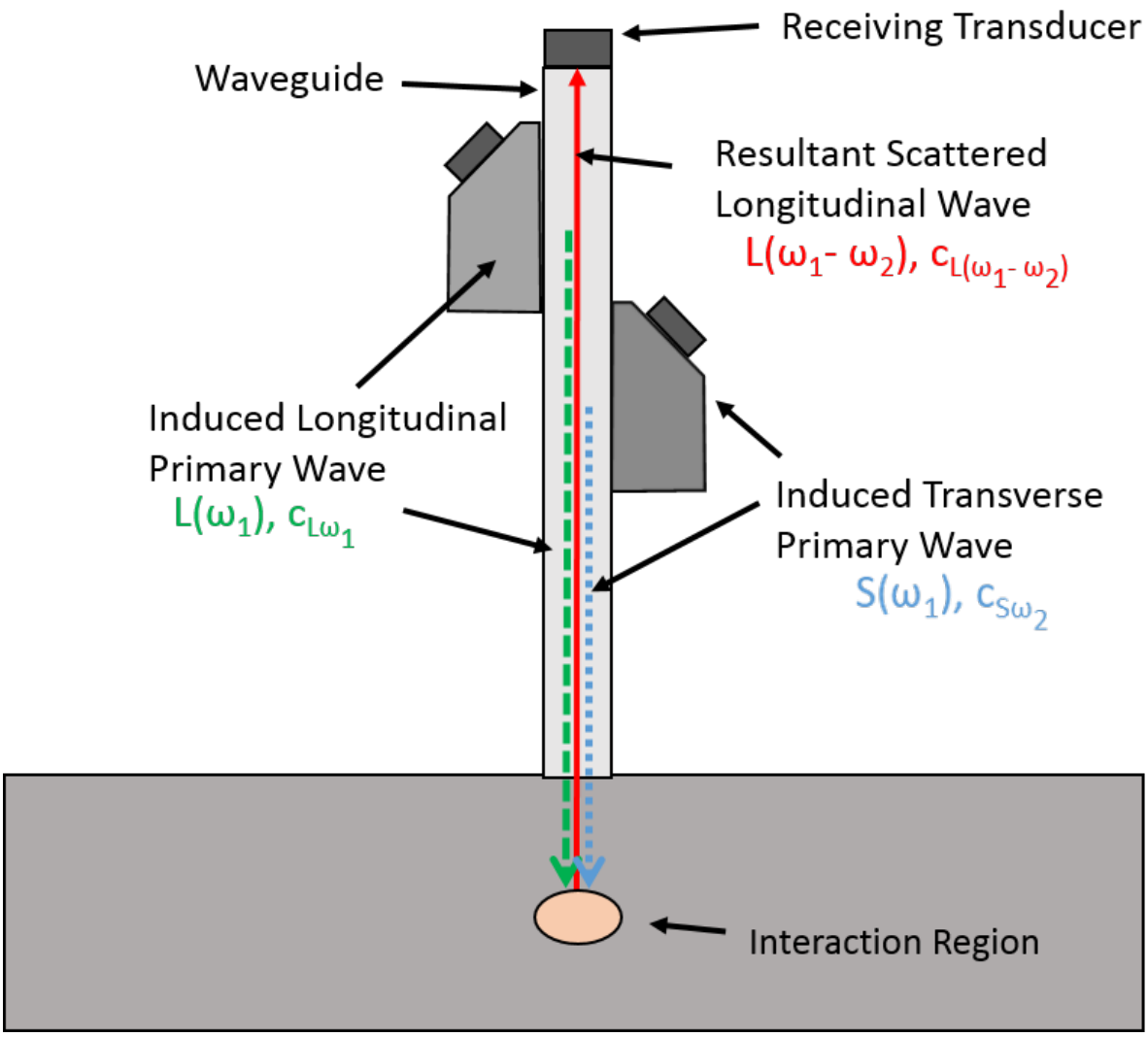

Figure 7.2: Schematic representation of a potential alternative configuration for single sided nonlinear interrogation of HTHA using a wave guide and angled wedges.

inducing waves at an angle into the specimen, it is necessary to rely on beam spread for the collinear interaction to occur. Since the primary waves will be at critically refracted angles, it is necessary to have a wave guide thin enough to allow the primary waves to spread out. This can be accomplished if the interaction region is at a large enough distance. The primary waves will be collinear because critically refracted angles are used forcing the primary waves to travel approximately parallel to the surface of the wave guide. Note that this method requires a delicate balance between the thickness of the wave guide and the ability to create a collinear interaction. If the wave guide is too thin, lamb waves,

a type of plate wave, can be induced in the wave guide [48]. Lamb waves are a combination of shear and longitudinal wave modes which are not desired for this nonlinear interaction case. The wave guide must be thin enough to avoid lamb waves and thick enough to allow beam spread of the primary waves to overlap. Additionally, this configuration would require coupling both primary wave wedges and the wave guide itself to the test piece. Due to the number of coupled interfaces in this configuration, variability can be an issue while measuring independent trials. Lastly, the travel distance for the nonlinear scattered wave is drastically increased using this configuration. This can be an issue if a highly attenuative test piece or wave guides is used.

The methods described above provide a basis for using collinear wave mixing for single sided HTHA inspection. This method could provide a more versatile system for inspection since there is no need to account for wedges incident on the pressure vessel surface. The first method has transducers placed directly on to the pressure vessel wall, and the second method has transducers mounted to a wave guide which can be mounted to a pressure vessel wall. Each of these methods has potential to be utilized for nonlinear interrogation, and could prove to be a more versatile configuration as the inspection technique progresses.

REFERENCES

[1] M. McGovern, D. Balch, and H. Reis, "Non-destructive evaluation and characterization of high-temperature hydrogen attack in carbon steel pressure vessels," *Insight-Non-Destructive Testing and Condition Monitoring*, vol. 59, no. 1, pp. 11–16, 2017.

[2] D. J. Benac and P. McAndrew, "Reducing the risk of high temperature hydrogen attack (htha) failures," *Journal of failure analysis and prevention*, vol. 12, no. 6, pp. 624–627, 2012.

[3] U.S. Chemical Safety And Hazard Investigation Board, "Catastrophic rupture of heat exchanger," 2014.

[4] M. Mckimpson and P. G. Shewmon, "Initial hydrogen attack kinetics in a carbon steel," *Metallurgical Transactions A*, vol. 12, pp. 825–834, 1981.

[5] American Petroleum Institute, "Publication 941," 1977.

[6] D. Bray and R. Stanley, *Nondestructive evaluation (revised ed.)*. CRC Press, Boca Raton, FL, 1997.

[7] M. Urzendowski, "Avoiding htha failures: An owner-user perspective of the htha risk mitigation process-part 1," *Inspectioneering Journal*, pp. 26–29, 2013.

[8] P. Shewmon and P. Anderson, "Void nucleation and cracking at grain boundaries," *Acta materialia*, vol. 46, no. 14, pp. 4861–4872, 1998.

[9] J. Nowakowski, "Naphtha hydrotreater E-6600E failure," TOP Investogation, Tech. Rep., 2010.

[10] M. Nugent, T. Silfies, J. D. Dobis, and T. Armitt, "A review of high temperature hydrogen attack (htha) modeling, prediction, and non-intrusive inspection in refinery applications," 2017.

[11] D. H. Simpson, C. T. Chin, and P. N. Burns, "Pulse inversion doppler: a new method for detecting nonlinear echoes from microbubble contrast agents," *IEEE transactions on ultrasonics, ferroelectrics, and frequency control*, vol. 46, no. 2, pp. 372–382, 1999.

[12] V. E. Nazarov, L. A. Ostrovsky, I. A. Soustova, and A. M. Sutin, "Nonlinear acoustics of micro-inhomogeneous media," *Physics of the Earth and Planetary Interiors*, vol. 50, no. 1, pp. 65–73, 1988.

[13] W. H. Johnson, "on some remarkable changes produced in iron and steel by the action of hydrogen and acids," 1875.

[14] M. Whiteman and A. Troiano, "Hydrogen embrittlement of austenitic stainless steel," *Corrosion*, vol. 21, no. 2, pp. 53–56, 1965.

[15] T. Shiraga, "Hydrogen embrittlement of steel," *Corrosion Engineering*, vol. 60, no. 5, pp. 188–194, 2011.

[16] E. Fletcher and A. R. Elsea, "The effects of high-pressure, high-temperature hydrogen on steel," DMIC, Tech. Rep., 1964.

[17] P. G. Shewmon, "Hydrogen attack of carbon steel," *Metallurgical Transactions A*, vol. 7, pp. 279–286, 1976.

[18] D. Eliezer, "High-temperature hydrogen attack of carbon steel," *Journal of materials science*, vol. 16, no. 11, pp. 2962–2966, 1981.

[19] M. Urzendowski, "Avoiding htha failures: An owner-user perspective of the htha risk mitigation process-part 2," *Inspectioneering Journal*, pp. 9–12, 2014.

[20] A. S. Birring, D. G. Alcazar, G. J. Hendrix, and J. J. Hanley, "Method and means for detection of hydrogen attack by ultrasonic wave velocity measurements," 1990, uS Patent 4,890,496.

[21] R. Latiff and N. Fiore, "Ultrasonic attenuation and velocity in two-phase microstructures," *The Journal of the Acoustical Society of America*, vol. 57, no. 6, pp. 1441–1447, 1975.

[22] W. D. Wang, "Ultrasonic technique for inspection of weld and heat-affected zone for localized high temperature hydrogen attack," 2000, uS Patent 6,125,704.

[23] H. Willems and K. Goebbels, "Ultrasonic attenuation measurement using backscattering technique," in *Review of Progress in Quantitative Nondestructive Evaluation*. Springer, 1989, vol. 8A, pp. 1747–1753.

[24] A. S. Birring, M. Riethmuller, and K. Kawano, "Ultrasonic backscatter and phased arrays for detection of high temperature hydrogen attack," *Materials Evaluation*, vol. 63, no. 2, 2005.

[25] F. Murnaghan, "Finite deformation of an elastic body," 1951.

[26] D. S. Hughes and J. Kelly, "Second-order elastic deformation of solids," *Physical review*, vol. 92, no. 5, p. 1145, 1953.

[27] N. Shiren, "Nonlinear acoustic interaction in mgo at 9 gc/sec," *Physical Review Letters*, vol. 11, no. 1, p. 3, 1963.

[28] G. L. Jones and D. R. Kobett, "Interaction of elastic waves in an isotropic solid," *The Journal of the Acoustical society of America*, vol. 35, no. 1, pp. 5–10, 1963.

[29] F. R. Rollins Jr, "Interaction of ultrasonic waves in solid media," *Applied Physics Letters*, vol. 2, no. 8, pp. 147–148, 1963.

[30] V. Krasilnikov and L. Zarembo, "Nonlinear interaction of elastic waves in solids," *IEEE Transactions on Sonics and Ultrasonics*, vol. 14, no. 1, pp. 12–17, 1967.

[31] Y. Hiki and K. Mukai, "Ultrasonic three-phonon process in copper crystal," *Journal of the Physical Society of Japan*, vol. 34, no. 2, pp. 454–461, 1973.

[32] P. A. Johnson, T. J. Shankland, R. J. O'connell, and J. N. Albright, "Nonlinear generation of elastic waves in crystalline rock," *Journal of Geophysical Research: Solid Earth*, vol. 92, no. B5, pp. 3597–3602, 1987.

[33] P. A. Johnson and T. J. Shankland, "Nonlinear generation of elastic waves in granite and sandstone: Continuous wave and travel time observations," *Journal of Geophysical Research: Solid Earth*, vol. 94, no. B12, pp. 17 729–17 733, 1989.

[34] V. A. Korneev, K. T. Nihei, and L. R. Myer, "Nonlinear interaction of plane elastic waves," Lawrence Berkeley National Lab., CA (United States), Tech. Rep., 1998.

[35] V.A. Korneev and A. Demcenko, "Possible Second-Order Nonlinear Interactions of Plane Waves in an Elastic Solid," *Journal of Acoustical Society of America*, vol. 135, no. 2, pp. 591–598, (2013).

[36] A. J. Croxford, P. D. Wilcox, B. W. Drinkwater, and P. B. Nagy, "The use of non-collinear mixing for nonlinear ultrasonic detection of plasticity and fatigue," *The Journal of the Acoustical Society of America*, vol. 126, no. 5, pp. EL117–EL122, 2009.

[37] A. Demčenko, R. Akkerman, P. Nagy, and R. Loendersloot, "Non-collinear wave mixing for non-linear ultrasonic detection of physical ageing in pvc," *NDT & E International*, vol. 49, pp. 34–39, 2012.

[38] M. E. McGovern, "Non-destructive quantitative assessment of oxidation in aged and rejuvenated asphalt concrete pavements using a non-collinear wave mixing approach," Ph.D. dissertation, University of Illinois at Urbana-Champaign, 2016.

[39] G. Tang, M. Liu, L. J. Jacobs, and J. Qu, "Detecting localized plastic strain by a scanning collinear wave mixing method," *Journal of Nondestructive Evaluation*, vol. 2, no. 33, pp. 196–204, 2014.

[40] P. G. Shewmon, C. Richied, M. McKimpson, and M. Ransick, "Effect of hydrogen pressure on morphology of hydrogen attack," *Scripta Metallurgica*, vol. 14, no. 5, pp. 545–548, 1980.

[41] W. Sachse and Y.-H. Pao, "On the determination of phase and group velocities of dispersive waves in solids," *Journal of applied Physics*, vol. 49, no. 8, pp. 4320–4327, 1978.

[42] I. A. Viktorov, *Rayleigh and lamb waves: physical theory and applications (ultrasonic technology)*. Springer, 2014.

[43] A. Wydra, A. Chertov, R. G. Maev, C. Kube, H. Du, and J. Turner, "Grain size measurement of copper spot welding caps via ultrasonic attenuation and scattering experiments," *Research in Nondestructive Evaluation*, vol. 26, no. 4, pp. 225–243, 2015.

[44] M. McGovern and H. Reis, "Damage characterization in dimension limestone cladding using noncollinear ultrasonic wave mixing," *Optical Engineering*, vol. 55, no. 1, pp. 011 012–011 012, 2016.

[45] P. Shewmon, H. Lopez, and T. Parthasarathy, "Chemically driven cavity growth," *Scripta Metallurgica*, vol. 17, no. 1, pp. 39–43, 1983.

[46] T. Laha, R. Balasubramaniam, M. Mungole, A. Tewari, and R. Baligidad, "Microstructural evolution in iron aluminide fe-28al-2c after high-temperature hydrogen treatment," *Metallurgical and Materials Transactions A*, vol. 35, no. 6, pp. 1789–1798, 2004.

[47] D. Egle and D. Bray, "Measurement of acoustoelastic and third-order elastic constants for rail steel," *The journal of the Acoustical Society of America*, vol. 60, no. 3, pp. 741–744, 1976.

[48] J. Rose, *Ultrasonic Waves in Solid Media*. Cambridge University Press.